

## COMPARISON OF RADIO OBSERVATIONS AND NUMERICAL SIMULATIONS OF THE RADIO LOBES OF CYGNUS A

JOEL C. CARVALHO<sup>1</sup>

Space Telescope Science Institute, 3700 San Martin Drive, Baltimore, MD 21218; carvalho@dfte.umd.edu

RUTH A. DALY AND MATTHEW P. MORY

Department of Physics, Berks–Lehigh Valley College, Pennsylvania State University, Tulpehocken Road, Reading, PA 19610;  
rdaly@psu.edu, mmory@srtdg.com

AND

CHRISTOPHER P. O'DEA

Department of Physics, Rochester Institute of Technology, 54 Lomb Memorial Drive, Rochester, NY 14623; odea@cis.rit.edu

Received 2004 May 20; accepted 2004 October 16

### ABSTRACT

We present a comparison of radio observations of the powerful archetypal radio galaxy Cyg A and two-dimensional numerical hydrodynamic simulations. We characterize some global trends in the observed radio properties and compare them with the properties of a simulated radio source. The observational results are the following. The width of the observed surface brightness distribution perpendicular to the source axis can be well characterized by a Gaussian over most of the length of the source. The ratio of the Gaussian FWHM to the second moment is fairly constant along the source, with an average value of about 2.5, indicating that they give roughly consistent measurements of the source width. The average observed surface brightness, estimated pressure, and estimated minimum-energy  $B$ -field decrease with distance from the hot spots. We find evidence for significant structure in the estimated cross-sectional slices of the emissivity. The numerical results are the following. Jets propagating in a constant-density atmosphere decelerate with time. Thus, the estimated dynamical age of the source is greater than the actual age of the source. For a source similar to Cyg A, the difference is about a factor of 2. The second moment gives an accurate representation of the “true” width of the simulated source. The Gaussian FWHM tends to be about 40% larger than the true width and can be systematically in error if the surface brightness exhibits multiple peaks. We suggest that the ratio of the Gaussian FWHM to the second moment may be a diagnostic of the emissivity profile in the lobes. The simulations can qualitatively reproduce the overall observed morphology, the behavior of the cross sections in surface brightness, the decline in surface brightness with distance from the hot spots, and the width of the lobes. This suggests that the two-dimensional simulations give a reasonable representation of the properties of Cyg A.

*Subject heading:* galaxies: active — galaxies: individual (Cyg A) — galaxies: jets — hydrodynamics — intergalactic medium — radio continuum: galaxies

### 1. INTRODUCTION

The primary physical processes in large powerful Faranoff-Riley (FR) II radio galaxies are still poorly understood. There is a consensus that these sources are powered by two oppositely directed highly collimated outflows from an active galactic nucleus (AGN), resulting in shocks and radio emission (Scheuer 1974; Blandford & Rees 1974). It is clear that the youngest populations of relativistic electrons are located near the radio hot spots at the extremities of the source (e.g., Leahy et al. 1989; Carilli et al. 1991; Alexander & Leahy 1987). Beyond this, differences of opinion begin to emerge.

It is important to understand the physical processes that shape the observed radio emission of a source. If these could be identified and understood, it might be possible to use the observed source properties to determine the pressure, density, and temperature of the ambient gas and the beam power of the source. These could then be used to probe the evolution of source environments with redshift and the evolution of AGN properties, such as jet power. These, in turn, would suggest

the circumstances that lead to AGN activity, and the role of environment in both triggering (perhaps via mergers or close encounters) and then constraining (through the gaseous environment) the radio properties of a source.

Much effort has been spent on analysis of multifrequency radio observations of radio galaxies (e.g., as summarized in Leahy 1991) and independently on numerical simulations of radio galaxies (e.g., Norman et al. 1982; Lind et al. 1989; Clarke et al. 1989; Hardee & Norman 1990; Falle 1991; Clarke & Burns 1991; Cioffi & Blondin 1992; Loken et al. 1992; Mioduszewski et al. 1997; Marti et al. 1997; Komissarov & Falle 1997, 1998; Rosen et al. 1999; Carvalho & O’Dea 2002a, 2002b).

Here we attempt to bridge these two fields by directly comparing radio images of the archetypal radio galaxy Cyg A with the results of two-dimensional hydrodynamic simulations of a source that is expected to be similar to Cyg A. Our goal is to explore the behavior of global observed properties and relate these to intrinsic properties of the underlying flows.

### 2. RADIO OBSERVATIONS AND DATA ANALYSIS

Two observations of Cyg A are studied in detail. The 151 MHz radio image from Leahy et al. (1989) was kindly provided to us

<sup>1</sup> Departamento de Física, UFRN, C.P. 1661, CEP 59072-970, Natal RN, Brazil.

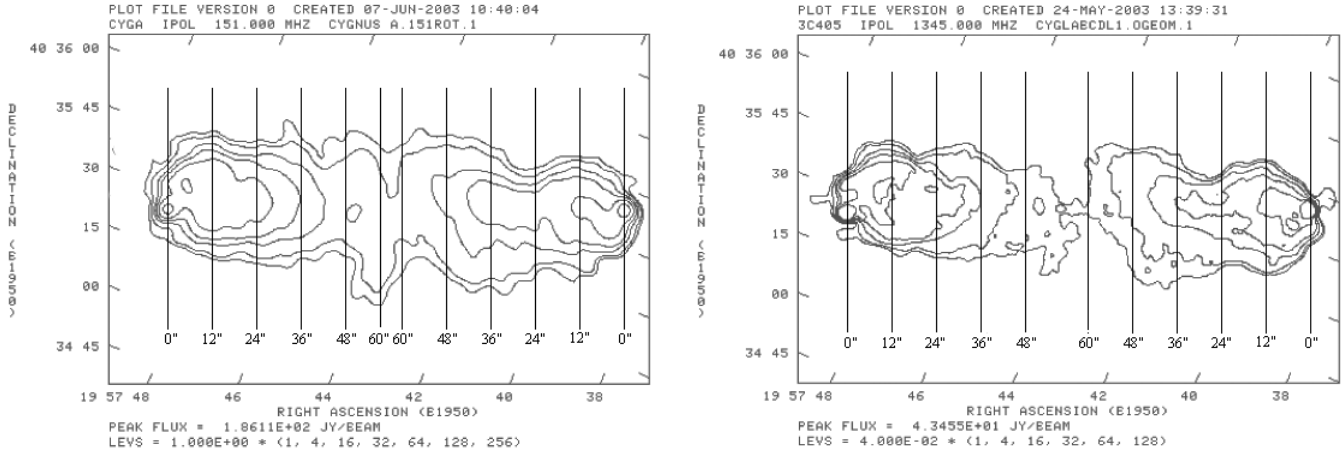


FIG. 1.—Examples of cross-sectional slices used to define the surface brightness profiles shown in Fig. 2 for the 151 MHz data (*left*) and the 1345 MHz data (*right*). The distance of the slice from the hot spot is indicated at the bottom of the slice. The images have been rotated slightly for ease of display. The left side is the southeast lobe, and the right side is the northwest lobe.

by Paddy Leahy, and the 1345 MHz image from Carilli et al. (1991) was kindly provided to us by C. Carilli. The 151 MHz image, obtained with MERLIN, has an angular resolution of  $3''$  and mean and rms noise levels of  $0.1$  and  $0.3$  Jy beam $^{-1}$ , respectively. The 1345 MHz image, obtained with the Very Large Array, has an angular resolution of  $1''.36$  and mean and rms noise levels of  $0.01$  and  $0.01$  Jy beam $^{-1}$ , respectively.

### 2.1. Surface Brightness Profiles and Gaussian Widths

The FITS images of the source at 151 and 1345 MHz were rotated in an identical manner so that the hot spots lay on a horizontal line. The hot spot–hot spot axis was taken to be a symmetry axis of the source. Using AIPS and auxiliary programs, vertical slices of surface brightness perpendicular to the hot spot symmetry axis were taken at 1 pixel intervals of the FITS image, as illustrated in Figure 1. Each surface brightness profile was then studied in detail. The distance to each slice is measured in arcseconds relative to the hot spot on each

side of the source, increasing as we move in toward the source center.

Each slice profile was fitted with a Gaussian curve to determine the FWHM of the best-fitting Gaussian. In these fits, we included the radio data above a threshold of the mean plus 3 times the rms noise level of each image; data below this level were removed. These cuts were taken at  $1$  Jy beam $^{-1}$  for the 151 MHz image and  $0.04$  Jy beam $^{-1}$  for the 1345 MHz image.

The radio surface brightness profiles and best-fit Gaussian curves are shown at integral intervals of  $3''$  (the FWHM of the 151 MHz image) in Figures 2–5 for the 151 and 1345 MHz data and for each side of the source. Generally, the Gaussian fits provide a good fit to the profiles; occasionally, the edges of the profiles drop more steeply than the wings of the Gaussian fit.

The FWHM values of these Gaussian fits are shown as a function of slice distance from the hot spot at 151 and 1345 MHz in Figure 6. The errors on the Gaussian widths are much smaller

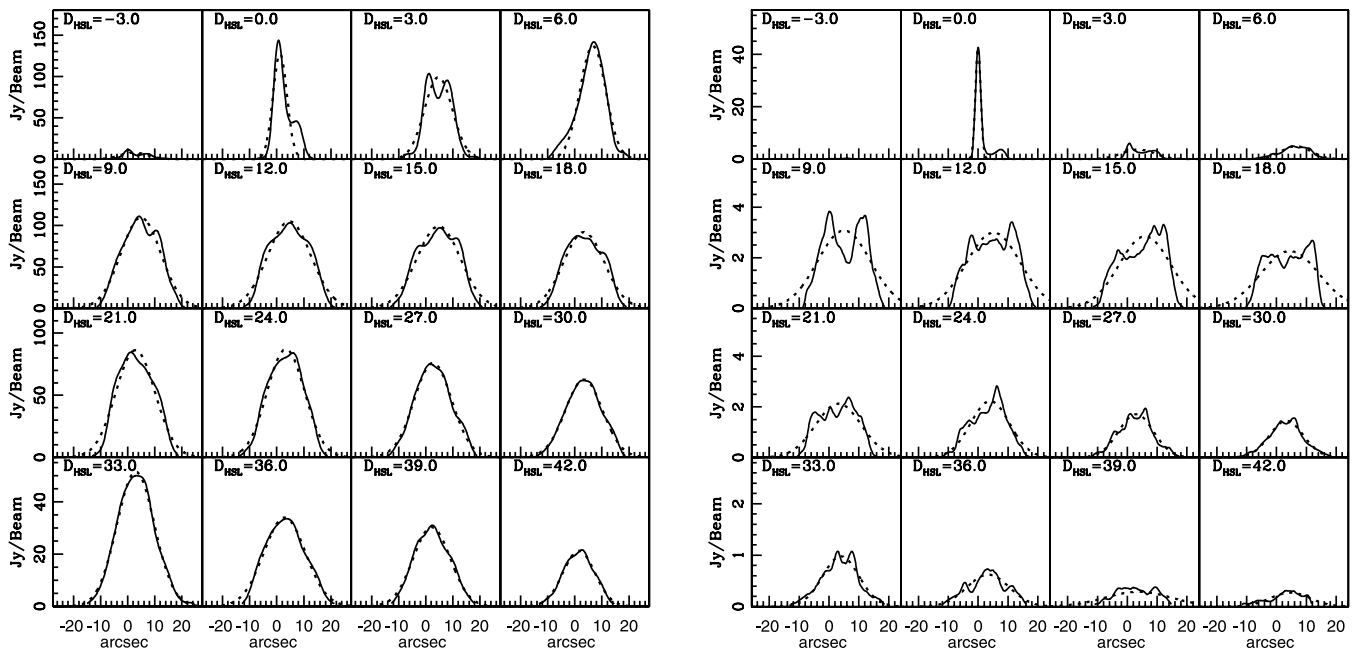


FIG. 2.—Cross-sectional surface brightness profiles (*solid lines*) and Gaussian fits (*dashed lines*) for the left side of Cyg A at 151 (*left*) and 1345 MHz (*right*). The distance of the slice from the hot spot is indicated for each slice.

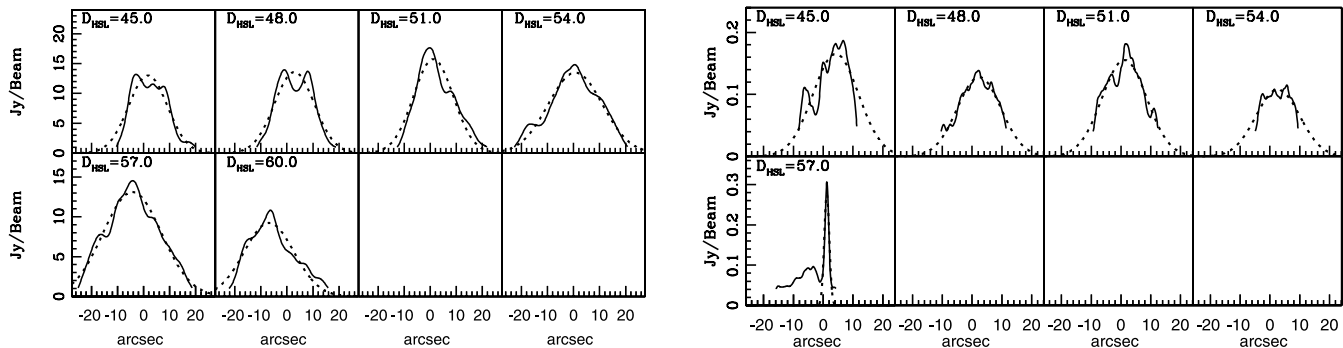


FIG. 3.—Continuation of the cross-sectional surface brightness profiles and Gaussian fits for the left side of Cyg A at 151 (*left*) and 1345 MHz (*right*).

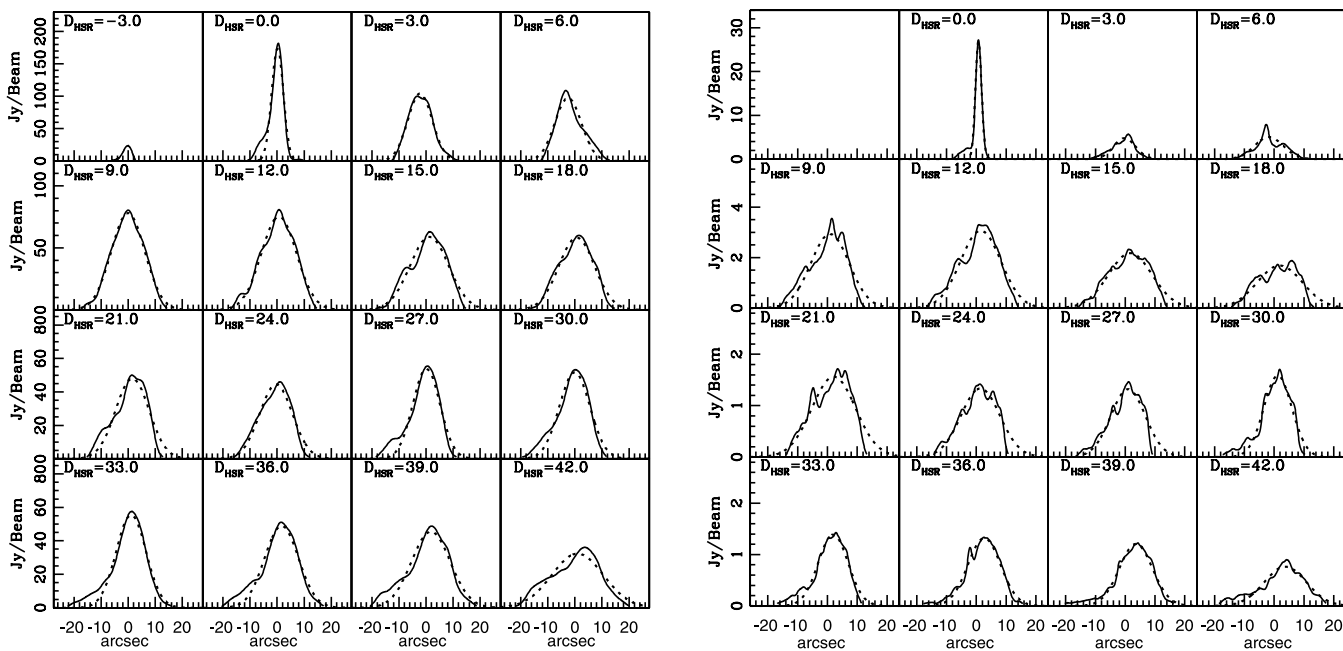


FIG. 4.—Same as Fig. 2, but for the right side of Cyg A.

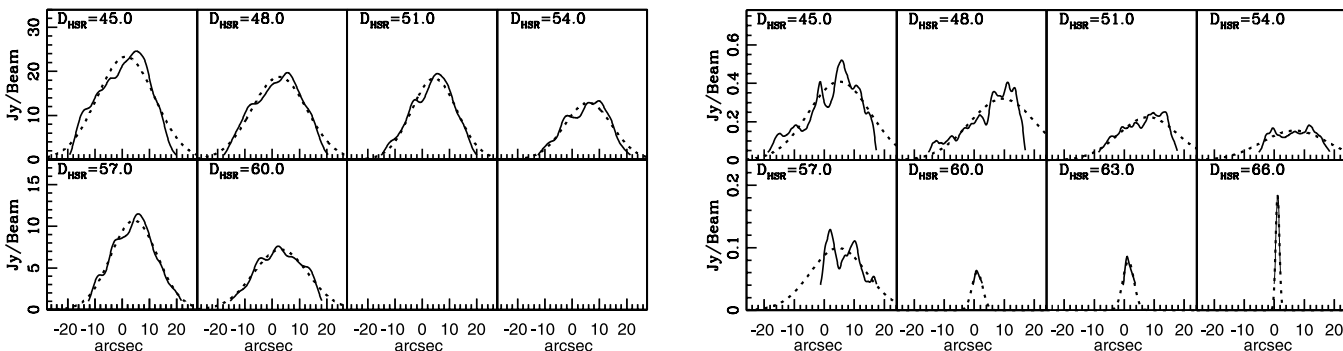


FIG. 5.—Same as Fig. 3, but for the right side of Cyg A.

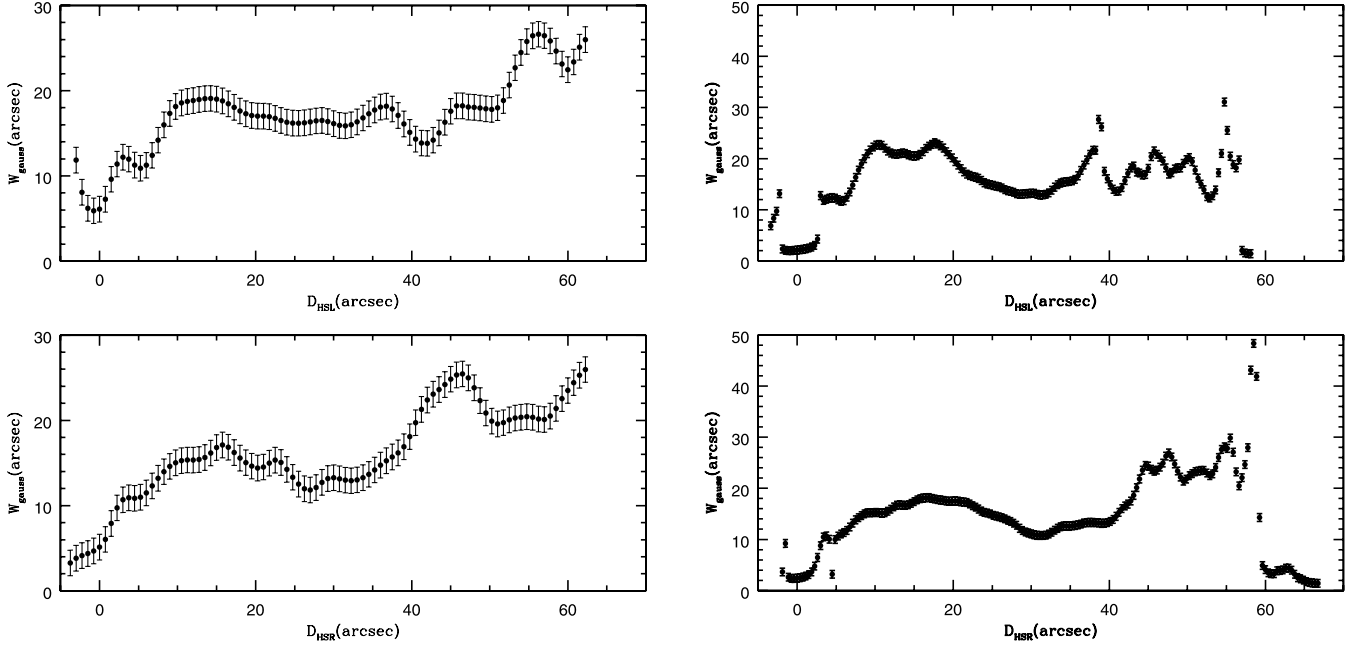


FIG. 6.—FWHM of the best-fit Gaussian as a function of slice distance from the hot spot at 151 (*left*) and 1345 MHz (*right*). *Top*, Results from the left side of the source; *bottom*, results from the right side.

than the FWHM of the radio observations, so the  $1\sigma$  error bar on the FWHM of the Gaussian was taken to be half the FWHM of the observing beam. Thus, an uncertainty of  $1''.5$  for the 151 MHz data and  $0''.7$  for the 1345 MHz data was adopted as the uncertainty of the Gaussian widths.

The ratios of the best-fit Gaussian widths at 151 and 1345 MHz are shown in Figure 7. The fact that this ratio is unity over most of the source is reassuring and suggests that to first order the 151 and 1345 MHz data define a similar source shape and structure. The average value of the ratio for the left and right sides of the source, respectively, are  $W_{151}/W_{1345} = 0.94 \pm 0.01$  and

$0.90 \pm 0.01$  when all the data are included; when only data with hot spot distances between  $6''$  and  $48''$  are included, these average values are  $0.92 \pm 0.01$  and  $1.01 \pm 0.01$  for the left and right sides of the source, respectively.

## 2.2. The First and Second Moments

Two other measures of source structure are the first and second moments of the cross-sectional surface brightness profiles described above. These were obtained using the standard expressions  $\bar{x} = \sum x_i S_i / \sum S_i$  and  $(\sum S_i [x_i - \bar{x}]^2 / \sum S_i)^{1/2}$ , where  $S_i$  is the surface brightness at the point  $x_i$ , shown on the surface

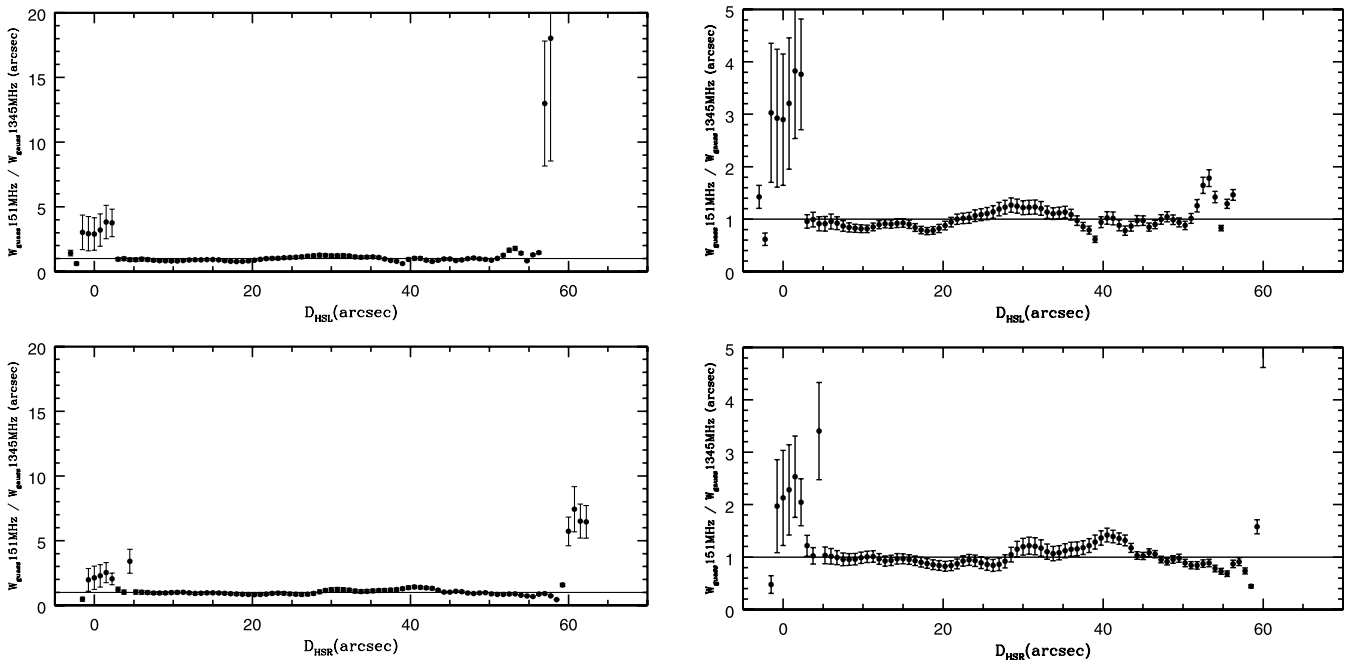


FIG. 7.—Ratio of the FWHM obtained at 151 MHz to that obtained at 1345 MHz. A more narrowly focused view is shown on the right.

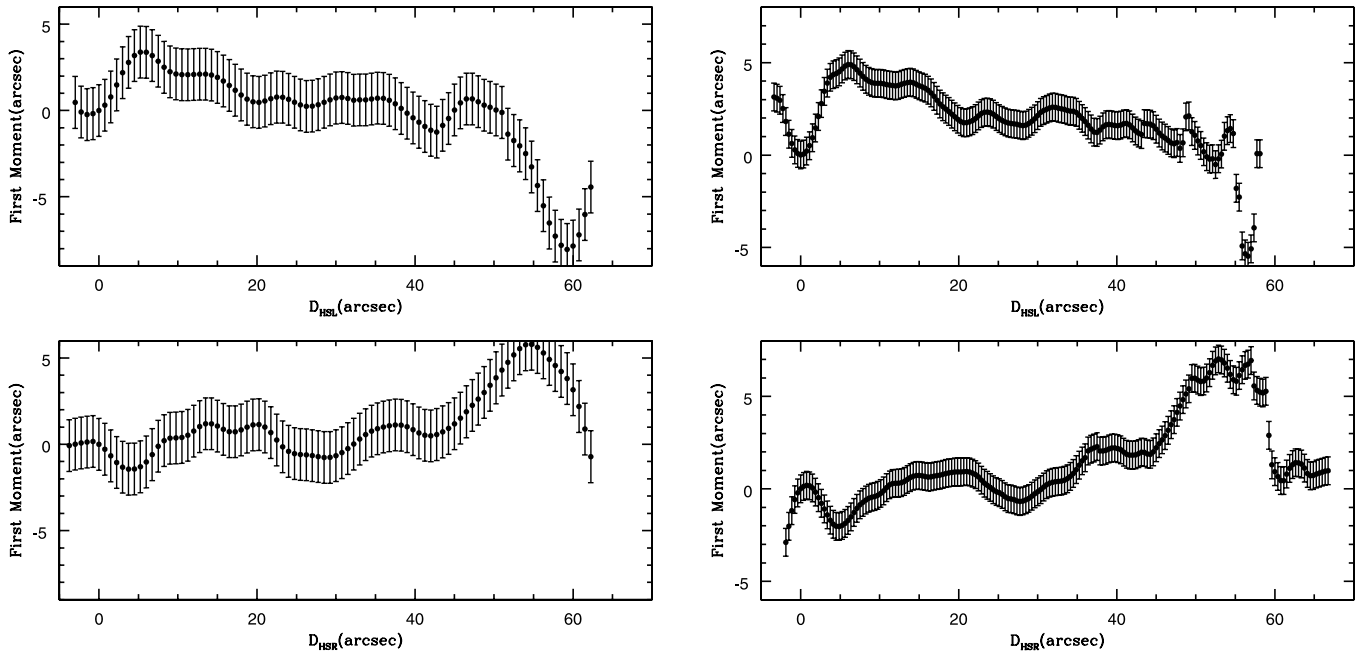


FIG. 8.—First moment of the cross-sectional surface brightness profiles as a function of distance from the hot spot for the 151 MHz data (*left*) and the 1345 MHz data (*right*). *Top*, Results from the left side of the source; *bottom*, results from the right side of the source.

brightness axis and  $x$ -axis in Figures 2–5. In Figures 8 and 9 these are plotted as a function of the slice distance from the hot spot. The uncertainty of the first moment is taken to be half the beam width, as above.

The first moment is a measure of the location of the surface brightness-weighted central axis of the source. In the 151 and 1345 MHz data, we see a varying displacement (or wandering) of the surface brightness-weighted source axis that is small compared with the Gaussian FWHM of the bridge at similar bridge locations. The first moment can be affected by the jet that is apparent in the radio gray-scale images, and it is interesting

that the deviations of the first moment from zero (the value expected for a perfectly cylindrical symmetric source) are in the opposite sense for the right and left side of the source, which could be influenced in part by any wobbling of the outflow axis of the jets. A detailed analysis indicates, however, that there is not an exact correspondence between the deviations of the first moment on the two sides of the source.

The second moment is another measure of the bridge width and is shown in Figure 9. The bridge width as measured by the best-fit Gaussian and the second moment are compared in Figure 10, which shows the ratio of the best-fit Gaussian

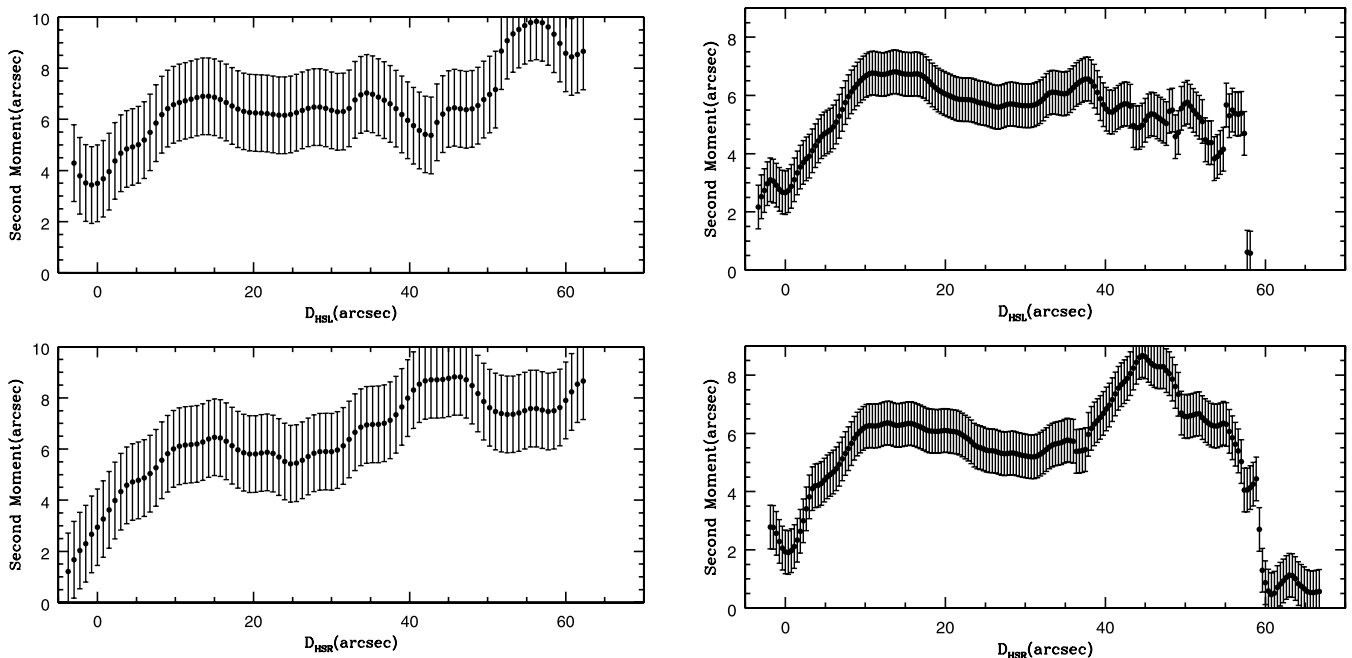


FIG. 9.—Same as Fig. 8, but for the second moment.

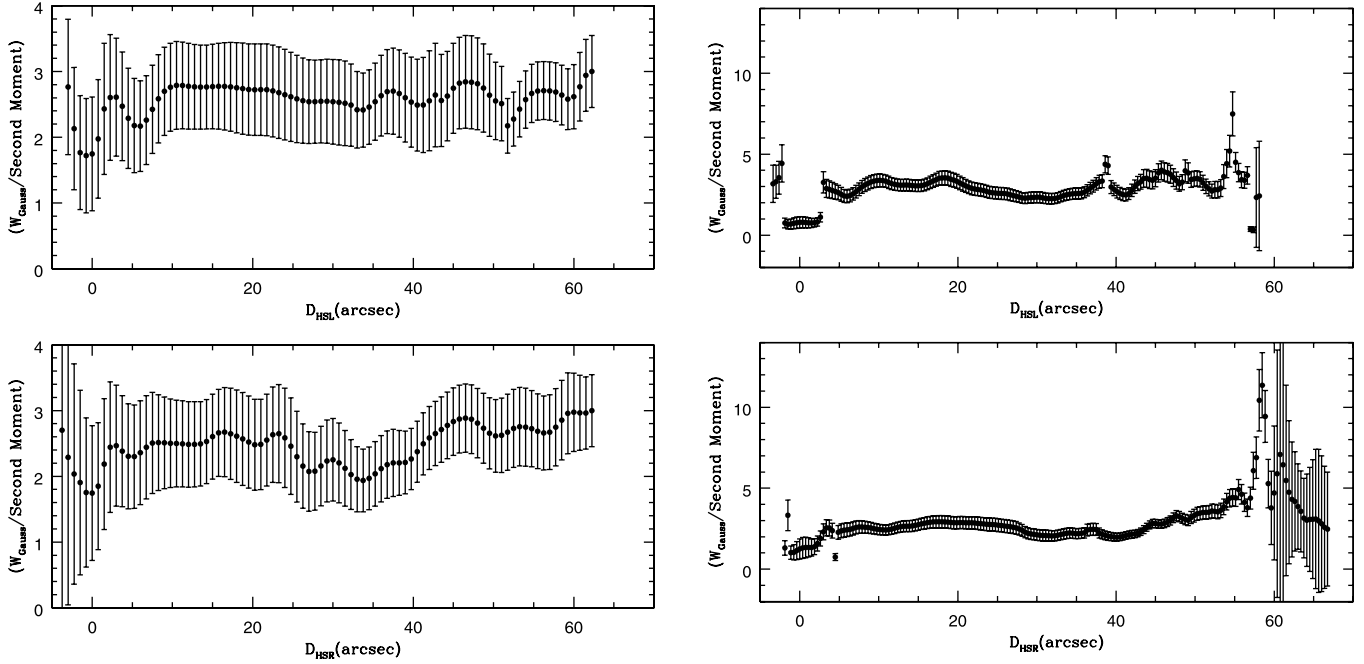


FIG. 10.—Ratio of the Gaussian FWHM to the second moment as a function of distance from the hot spot for the 151 MHz data (*left*) and the 1345 MHz data (*right*). *Top*: Measurements from the left side of the source. The average values are  $2.59 \pm 0.07$  and  $2.45 \pm 0.03$  for the 151 and 1345 MHz data, respectively. *Bottom*: Measurements from the right side of the source. The average values are  $2.49 \pm 0.07$  and  $2.53 \pm 0.03$  for the 151 and 1345 MHz data, respectively.

FWHM to the second moment. For the 151 MHz data, this ratio is  $2.59 \pm 0.07$  for the left side of the source and  $2.49 \pm 0.07$  for the right side of the source, while for the 1345 MHz data, this ratio is  $2.45 \pm 0.03$  and  $2.53 \pm 0.03$  for the left and right sides, respectively. The fact that the ratio is similar over most of the source suggests that either method may be used to estimate the bridge width. The physical interpretation of the numerical value of the ratio is discussed in § 3 (numerical simulations). Note that the ratio  $W_G/W_2$  discussed in § 3.4, obtained from numerical

simulations, is half the value stated here, since  $W_2$  is twice the bridge radius indicated by the second moment.

### 2.3. The Average Surface Brightness along the Bridge

The average surface brightness of each cross-sectional surface brightness profile is shown in Figure 11. This is obtained by summing the total area under a particular surface brightness profile (see Figs. 2–5) and dividing by the FWHM of the best-fit Gaussian curve,  $W_G$ :  $\bar{S} = \sum S_i \Delta x / W_G$ , where  $S_i$  is the surface

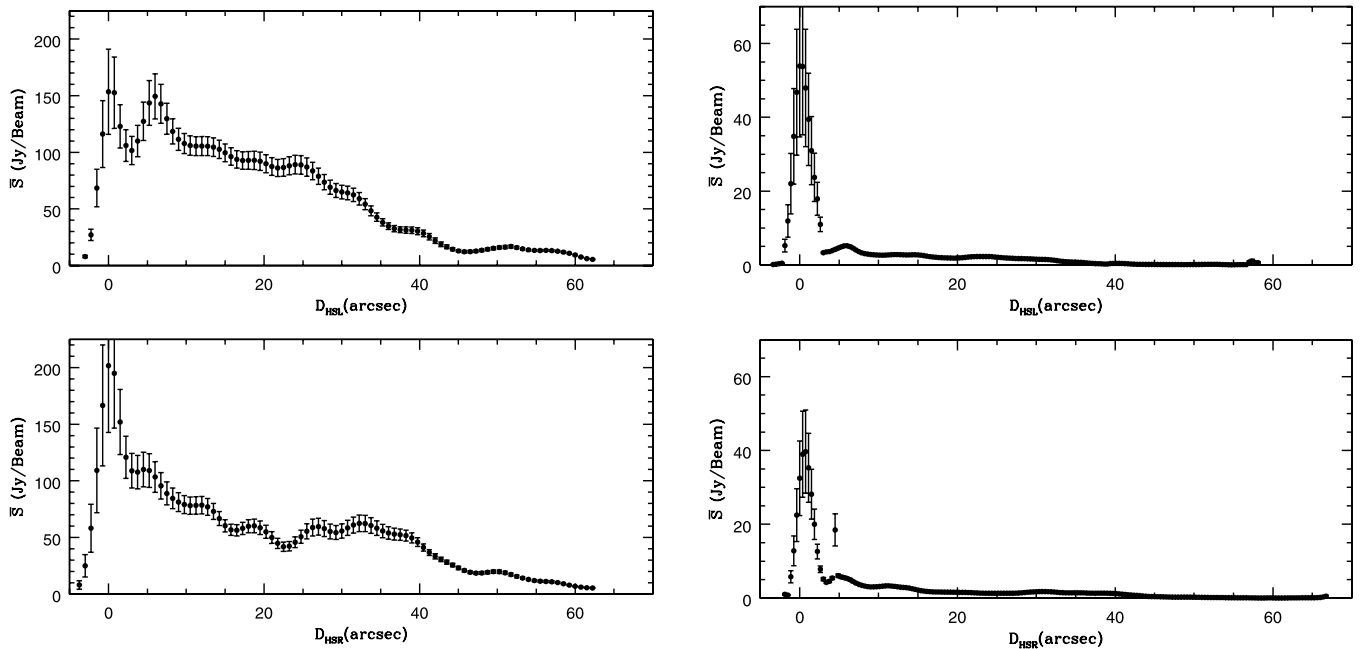


FIG. 11.—Average surface brightness in a cross-sectional surface brightness slice as a function of distance from the hot spot for the 151 MHz data (*left*) and the 1345 MHz data (*right*), obtained by assuming that the diameter of the bridge at each distance from the hot spot can be approximated by the FWHM of the best-fit Gaussian. *Top*, Results from the left side of the source; *bottom*, results from the right side of the source.

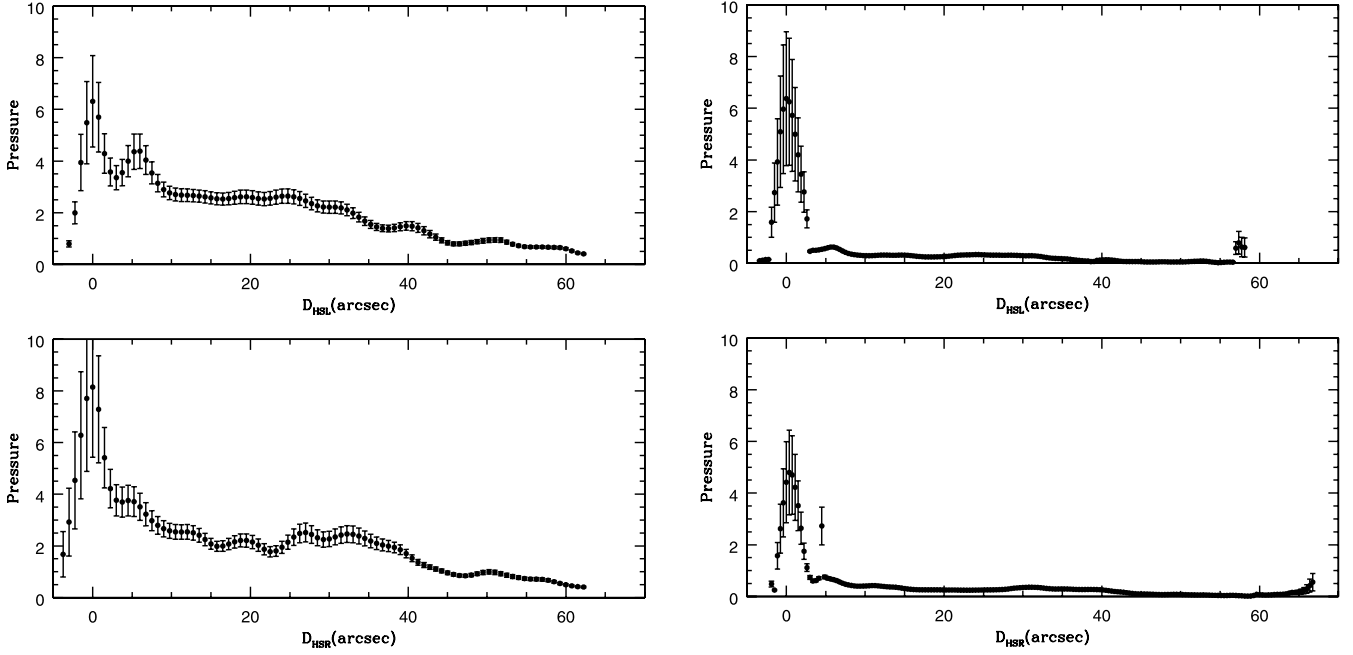


Fig. 12.—Average pressure in a cross-sectional surface brightness slice as a function of distance from the hot spot for the 151 MHz data (*left*) and the 1345 MHz data (*right*). The pressure for the 151 MHz data has units of  $1.2 \times 10^{-11}(1.33b^{-1.5} + b^2)$  ergs  $\text{cm}^{-3}$ , where  $b$  parameterizes the offset from minimum-energy conditions. For minimum-energy conditions,  $b = 1$ , and the normalization factor or pressure unit for the 151 MHz data is  $2.8 \times 10^{-11}$  ergs  $\text{cm}^{-3}$ , while for a field strength that is about 0.25 times the minimum-energy value, the normalization is  $1.3 \times 10^{-10}$  ergs  $\text{cm}^{-3}$ . The normalization factor for the 1345 MHz data is  $10^{-10}(1.33b^{-1.5} + b^2)$  ergs  $\text{cm}^{-3}$ . For minimum-energy conditions, the pressure unit for the 1345 MHz data is  $2.4 \times 10^{-10}$  ergs  $\text{cm}^{-3}$ , while for  $b = 0.25$ , the pressure unit is  $1.1 \times 10^{-9}$  ergs  $\text{cm}^{-3}$ . *Top*, Measurements from the left side of the source; *bottom*, measurements from the right side of the source.

brightness for the  $i$ th point and  $\Delta x$  is the interval along the  $x$ -axis around the point  $i$ . Thus, the units of the average surface brightness are  $\text{Jy beam}^{-1}$ . Numerical simulations (see § 3) indicate that  $W_G$  is a good estimate of the bridge diameter, suggesting that the surface brightness values obtained and shown in Figure 11 do not need to be renormalized.

The uncertainty of the average surface brightness is obtained by adding the rms noise level of the image in quadrature with the beam width:  $(\delta\bar{S}/\bar{S})^2 = (\text{rms}/\bar{S})^2 + (\theta_b/2W_G)^2$ , where  $\theta_b$  is the FWHM of the observing beam; recall that the uncertainty on the Gaussian width is taken to be half the beam size.

The contrast between the hot spots and the bridge is much higher for the 1345 MHz data than it is for the 151 MHz data, and the values of  $\bar{S}$  differ substantially for the data sets. But, once we move beyond the hot spots into the bridge region, the profile of the average surface brightness along the bridge axis is similar for the two frequencies, which can be seen in Figure 11.

#### 2.4. The Average Pressure and Minimum-Energy Magnetic Field along the Bridge

The average bridge pressure for each slice is plotted as a function of distance from the hot spot on each side of the source in Figure 12. This is a “minimum energy” pressure (Burbidge 1956) in the sense that it is obtained using the equation  $P = (\bar{S}/W_G)^{4/7}$  (see Figs. 2–5). Thus, the units of pressure are  $(\text{Jy arcsec}^{-1})^{4/7}$ . To convert this to the physical units ergs  $\text{cm}^{-3}$  and thus obtain the normalization factor to apply to the pressure presented, we note that the pressure is simply related to the minimum-energy magnetic field (e.g., Wan et al. 2000) as  $P = (1.33b^{-1.5} + b^2)B^2/(24\pi)$ , where  $B$  is the minimum-energy magnetic field strength and  $b$  parameterizes the offset from minimum-energy conditions; the true field strength is  $bB$ . As described below, the minimum-energy magnetic field strength estimated using the 151 MHz data has a normalization factor of

30  $\mu\text{G}$ , so the normalization factor for the pressure estimated using the 151 MHz data is about  $1.2 \times 10^{-11}(1.33b^{-1.5} + b^2)$  ergs  $\text{cm}^{-3}$ , or about  $2.8 \times 10^{-11}$  ergs  $\text{cm}^{-3}$  for  $b = 1$ , or about  $1.3 \times 10^{-10}$  ergs  $\text{cm}^{-3}$  for  $b = 0.25$ , as suggested by Carilli et al. (1991) and confirmed by Wellman et al. (1997a, 1997b) for the bridge region of Cyg A. At 1345 MHz the normalization factor for the pressure is  $10^{-10}(1.33b^{-1.5} + b^2)$  ergs  $\text{cm}^{-3}$ , or about  $2.4 \times 10^{-10}$  ergs  $\text{cm}^{-3}$  for  $b = 1$ , or about  $1.1 \times 10^{-9}$  ergs  $\text{cm}^{-3}$  for  $b = 0.25$ .

It is clear from Figure 12 that the minimum-energy magnetic fields computed for the bridge region using the 151 and 1345 MHz data are similar in magnitude and structure, while the pressures computed for the hot spots are considerably different, with the 1345 MHz data indicating a much higher pressure than the 151 MHz data.

The average minimum-energy magnetic field strength in each slice is obtained by taking the square root of the minimum-energy pressure,  $B = (\bar{S}/W_G)^{2/7}$ . The normalization factor is obtained using the standard expression for the minimum-energy magnetic field strength, assuming zero energy in relativistic protons, a filling factor of unity, a constant spectral index of unity, frequency cutoffs of 10 MHz and 100 GHz, and a cosmology with a value of Hubble’s constant of  $70 \text{ km}^{-1} \text{ s}^{-1} \text{ Mpc}$ , a normalized mean mass density today of  $\Omega_m = 0.3$ , and a cosmological constant of  $\Omega_\Lambda = 0.7$ . These parameters yield a normalization for the minimum-energy magnetic field strength for the 151 MHz data of about 30  $\mu\text{G}$  and a normalization factor of about 88  $\mu\text{G}$  for the 1345 MHz data. The minimum-energy magnetic field strengths are shown in Figure 13. Like the minimum-energy pressure, the minimum-energy magnetic field strengths across the bridge computed using the 151 and 1345 MHz data are quite similar in magnitude and structure, while the hot spot magnetic field indicated by the 1345 MHz data is much larger than that indicated by the 151 MHz data. One reason that

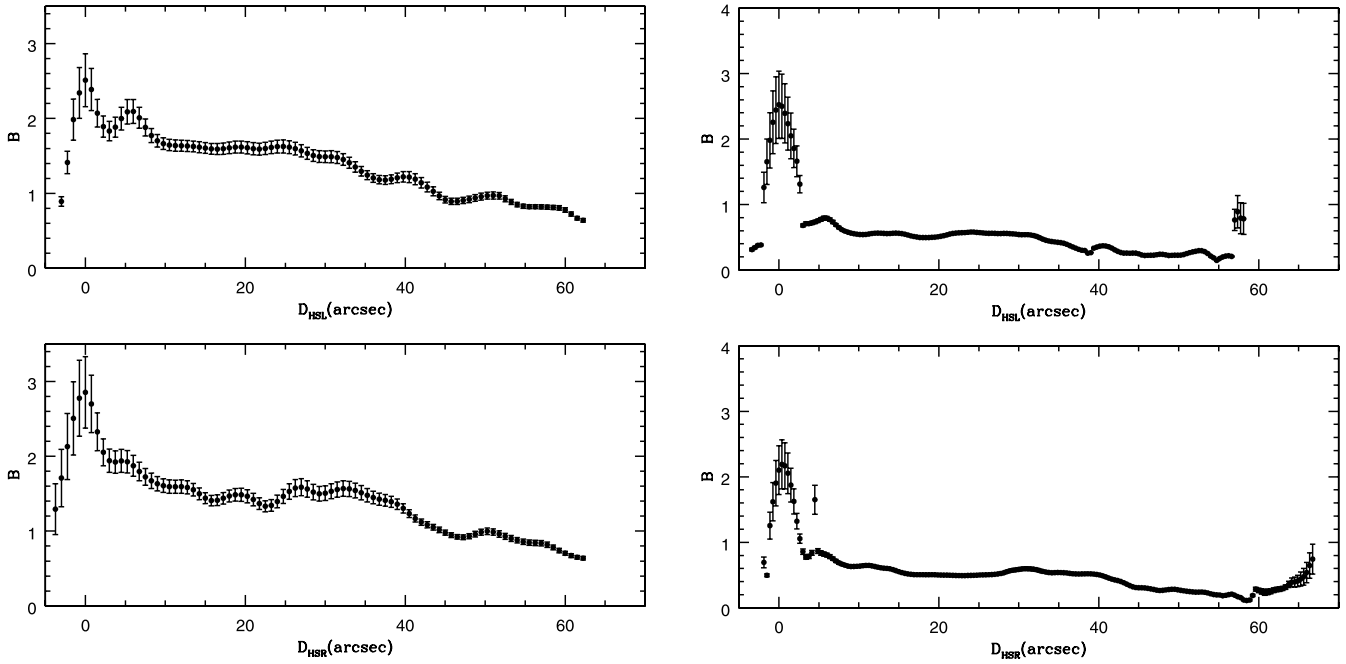


FIG. 13.—Average minimum-energy magnetic field strength in a cross-sectional surface brightness slice as a function of distance from the hot spot for the 151 MHz data (*left*) and the 1345 MHz data (*right*). The units of the minimum magnetic field strength for the 151 MHz data are  $30 \mu\text{G}$ , while those for the 1345 MHz data are  $88 \mu\text{G}$ . *Top*, Estimates from the left side of the source; *bottom*, estimates from the right side of the source.

the estimated pressure in the radio hot spots at 151 and 1345 MHz differs is that the magnetic field strengths and, hence, pressures have been estimated assuming a constant spectral index of unity. While this may be a reasonable estimate in the bridge region of the source, it is clearly not a good approximation in the hot spot region.

Note that the total pressure  $P$  in relativistic electrons and fields estimated assuming that this pressure is proportional to the square of the minimum-energy magnetic field implies that  $P \propto \epsilon^{4/7}$ , where  $\epsilon$  is the volume emissivity of the radio emission (see § 2.5). This follows from the fact that the radio surface

brightness  $S$  is obtained by integrating the emissivity along the source path length, so  $\bar{S} \sim \epsilon W_G$ . Thus,  $P = (\bar{S}/W_G)^{4/7}$ , which follows directly from the minimum-energy argument, implies that  $P \propto \epsilon^{4/7}$ . This is a good approximation whenever the true field strength is proportional to the minimum-energy magnetic field with a proportionality constant that is independent of position in the source.

2.5. The Radio Emissivity as a Function of Position

The emissivity, or energy emitted per unit volume per unit time at one particular frequency, can be obtained from the

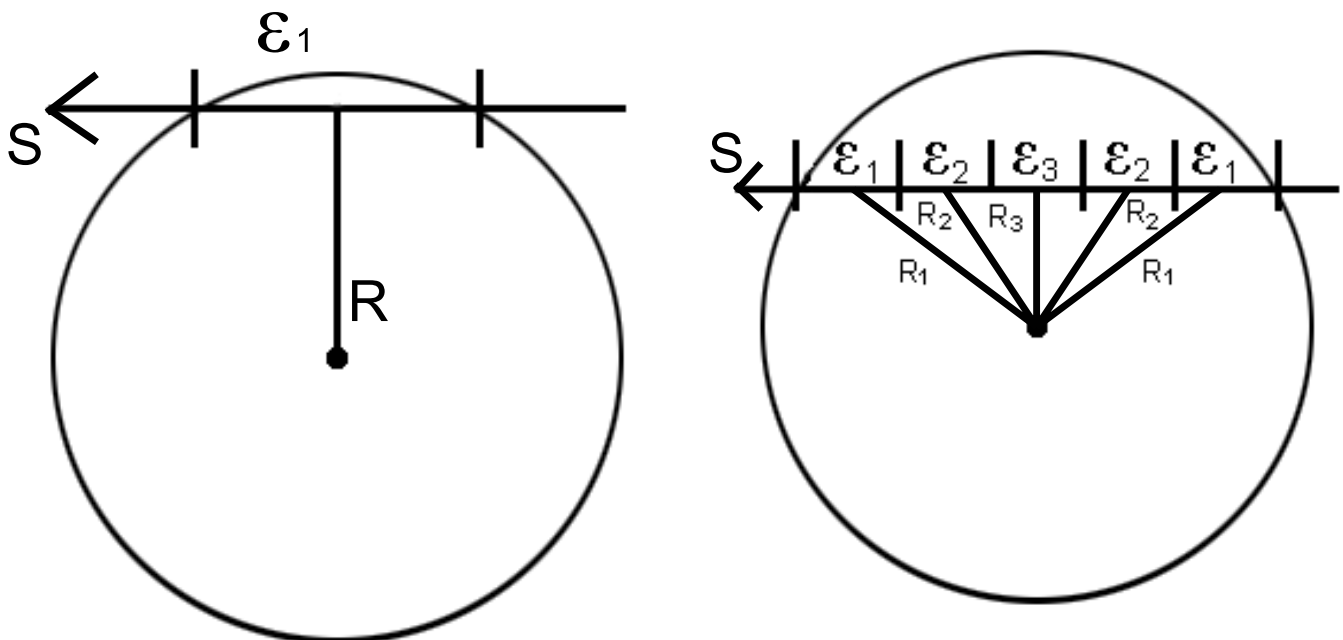


FIG. 14.—Method of obtaining the emissivity as a function of radial distance from the slice center.

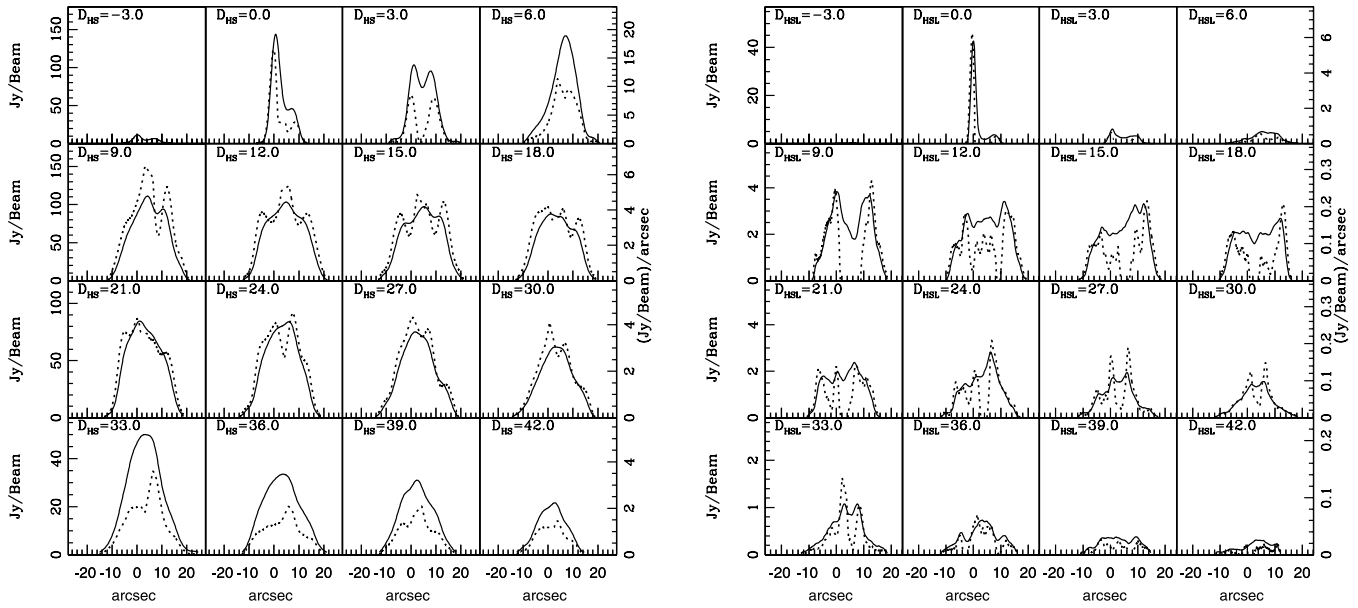


FIG. 15.—Radio emissivities (*dashed lines*) and cross-sectional surface brightness profiles (*solid lines*) for the 151 MHz data (*left*) and the 1345 MHz data (*right*) for the left side of Cyg A. The units for the 151 MHz data are  $1.8 \times 10^{-34}$  ergs $^{-1}$  cm $^{-3}$  Hz $^{-1}$ , while those for the 1345 MHz data are  $9.0 \times 10^{-34}$  ergs $^{-1}$  cm $^{-3}$  Hz $^{-1}$ .

surface brightness profiles shown in Figures 2–5. For a particular surface brightness profile, it is assumed that the emission is cylindrically symmetric, and that the diameter of the cylinder is equal to the total width of that profile (only data above the noise level of the mean+3 rms are included). Then, the emissivity as a function of radius from the center of the slice can be determined. This is done in the following way. The data point that is farthest from the center of the slice with a surface brightness above the noise level is used to determine the edge of the source. We move by a distance  $\Delta x$  to a position that is centered on  $R_1$  and compute the emissivity  $\epsilon_1$  at the point  $R_1$  by dividing the surface brightness at this point by the length of the chord through the circle at that point, as illustrated in Figure 14. We then have the emissivity  $\epsilon_1$  at all points that are at a distance  $R_1$  from the center of the cylinder for that slice. As we step in, the next surface brightness data point can be used to determine the emissivity  $\epsilon_2$  at a distance  $R_2$  from the center of the circle; this is done by accounting for the fact that the total surface brightness  $S_2$  includes contributions from  $\epsilon_1$  and  $\epsilon_2$ , as illustrated in Figure 14. This process is continued to obtain the emissivity at each distance  $R_n$  from the center of the axis of symmetry of the source and is valid to the extent that the slice possesses cylindrical symmetry.

The normalization for the volume emissivity  $\epsilon_\nu \equiv dE/(dV dt d\nu)$  can be obtained by noting that the emission

coefficient is  $j_\nu = \epsilon_\nu/(4\pi)$  for a volume element that emits isotropically, and the specific intensity is  $I_\nu = j_\nu \Delta y$ , where  $\Delta y$  is the length of the ray through the source shown in Figure 14. The observed specific intensity is  $I_{\nu o} = I_\nu(1+z)^{-3}$  and has units of Jy beam $^{-1}$ . By using these expressions, it is easy to show that the normalization factors for the emissivities shown in Figures 15–18 are  $1.8 \times 10^{-34}$  ergs $^{-1}$  cm $^{-3}$  Hz $^{-1}$  for the 151 MHz data and  $9.0 \times 10^{-34}$  ergs $^{-1}$  cm $^{-3}$  Hz $^{-1}$  for the 1345 MHz data.

These emissivities show significant structure, indicating that any given slice can have regions with very high and/or very low emissivities (or that the assumption of cylindrical symmetry is not valid for that slice). A relatively large change in emissivity is needed to produce a relatively small surface brightness feature. Some of the changes in emissivity suggest a channel or jetlike feature, which are suggested by either an emission feature or a cavity in the emissivity near the center of the slice. The variations in emissivity could be due to variations from cylindrical symmetry or to hydromagnetic waves, turbulence, or other effects.

### 3. CYG A VERSUS NUMERICAL SIMULATIONS

Here we present the results of two-dimensional numerical hydrodynamic simulations and compare them with the observational results for Cyg A. The advantage is that in the simulations we know the *intrinsic* properties of the “source.” The

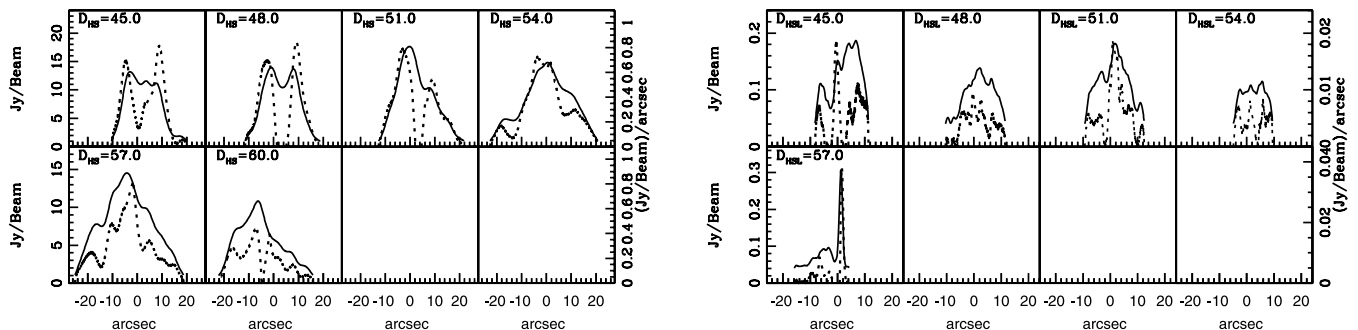


FIG. 16.—Continuation of the radio emissivities and cross-sectional surface brightness profiles for the left side of Cyg A.

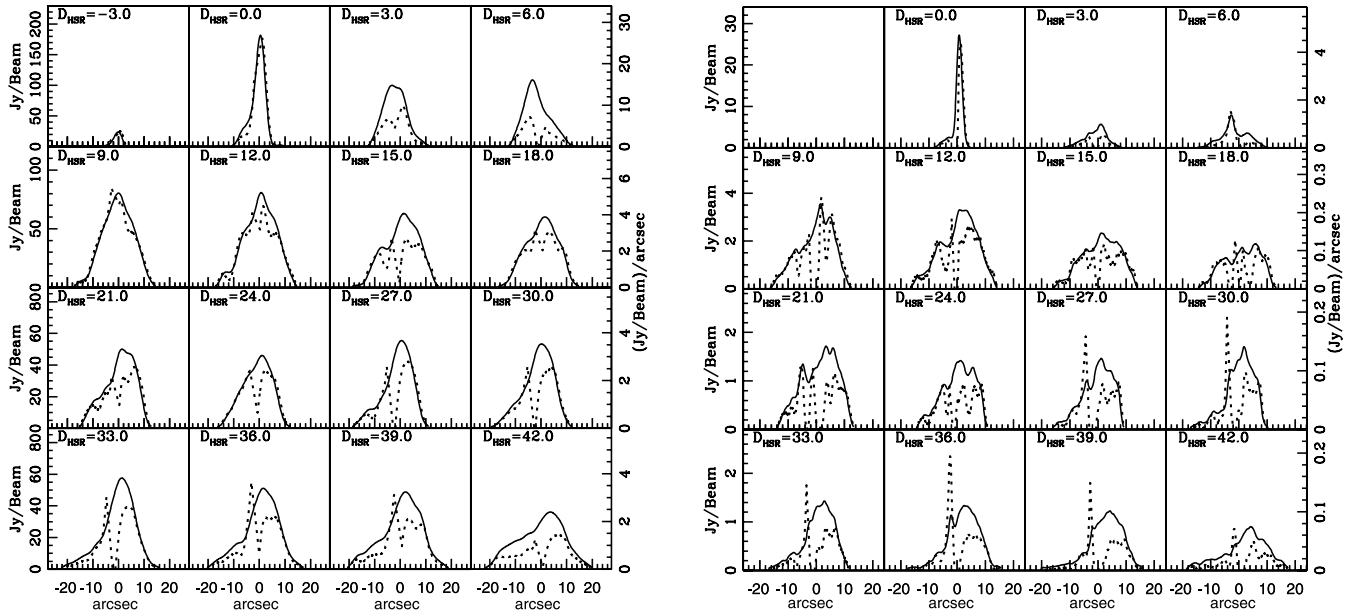


FIG. 17.—Same as Fig. 15, but for the right side of Cyg A.

disadvantage is that the simulations may not include all the relevant physics that occurs in real radio galaxies.

### 3.1. The Numerical Simulations

We have carried out axisymmetric hydrodynamic numerical simulations of light jets propagating in a constant-density atmosphere. The details of the simulations are discussed by Carvalho & O’Dea (2002a, 2002b). We have chosen not to include magnetic fields in the simulations. If the magnetic field is dominant, MHD simulations produce structures (e.g., the “nose cone”; Clarke et al. 1986; Lind et al. 1989) that do not appear to correspond to the observed radio structures in Cyg A. If the magnetic field is not dominant, the overall structure and dynamics of the source in the MHD simulation are similar to the case in which the magnetic field is absent. In addition, in a particle pressure-dominated source, the magnetic field distribution closely follows the distribution of gas pressure and density (Lind et al. 1989). Numerical simulations by Komissarov (1989) show that if the magnetic field is initially weak, it comes into equilibrium with the gas pressure near the “cocoon” boundary because the gas pressure drives the sideways expansion of the cocoon, and the gas is not able to cross the magnetic field lines.

Numerical simulation studies (e.g., Norman et al. 1982; Carvalho & O’Dea 2002a, 2002b; Krause 2003) indicate that

light jets inflate a cocoon whose width is inversely proportional to the density ratio ( $\eta$ ) between the jet and the ambient gas. The overexpanded bridge in Cyg A implies a very low value for  $\eta$  ( $<10^{-3}$ ). According to Alexander & Pooley (1996), an order-of-magnitude estimate of the jet density is  $\eta \sim 4 \times 10^{-5}$ . We ran a number of simulations in which we used  $\eta = 2 \times 10^{-4}$  and jet internal Mach number  $M = 10$  (run D01),  $\eta = 1 \times 10^{-4}$  and  $M = 11$  (run D02), and  $\eta = 1 \times 10^{-4}$  and  $M = 10$  (run D03). One of the reasons for doing so was to ensure that small changes in the jet parameters did not have a significant effect on the final result. Since the overall linear size of Cyg A is  $\sim 120$  kpc, we used a simulation grid with a physical dimension of 66 kpc in the direction of the source axis and a jet radius of 1 kpc. We expected that, as the bow shock in front of the jet head reached the end of the grid, the expanded cocoon would give a fair representation of the source lobe. We ran the simulations with several different grid widths (equivalent to 16.5, 33, and 49.5 kpc) to study the effect on the cocoon of the bow shock leaving the grid. In the largest grid (run D01), the entire source is contained in the grid, while in the smaller grids, the bow shock eventually leaves the grid laterally. We find that the details of the cocoon properties differ in these simulations, although the overall properties of the cocoons are similar. This gives us confidence in the results of simulations carried out in the narrower grids, which are computationally much less expensive.

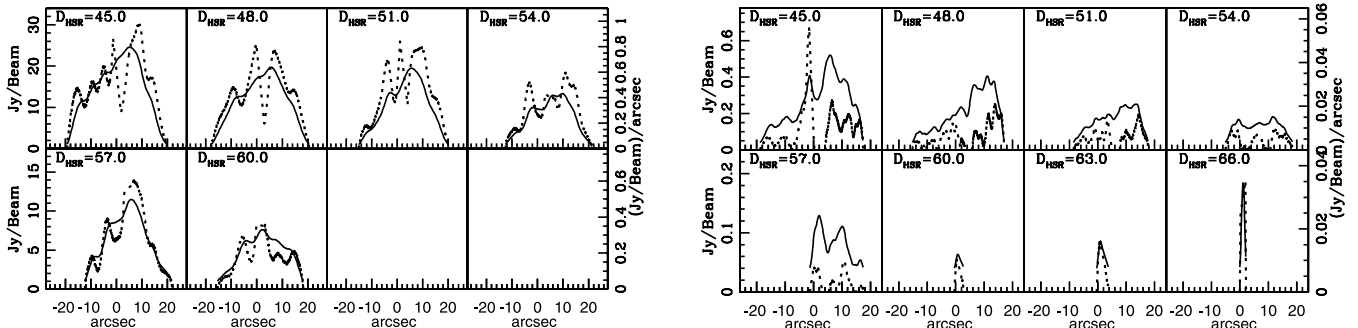


FIG. 18.—Same as Fig. 16, but for the right side of Cyg A.

D01

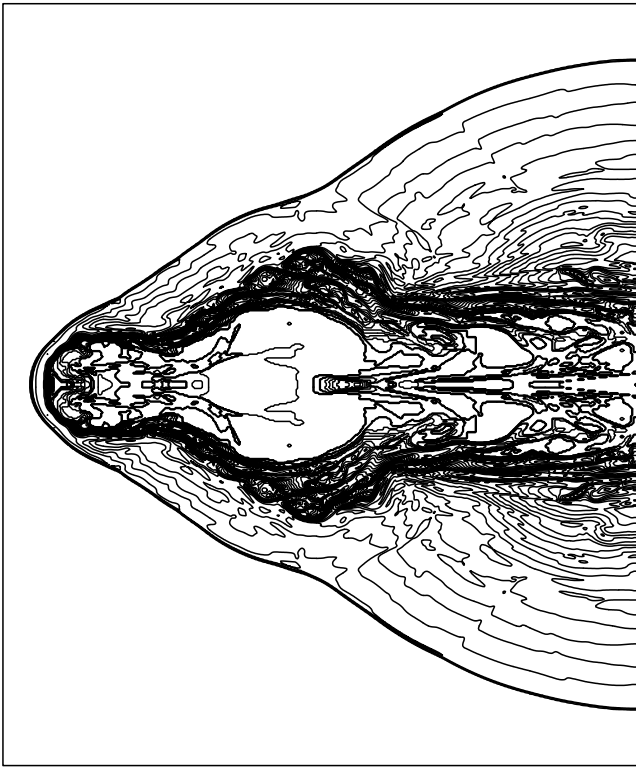


FIG. 19.—Density contour map of a jet propagating in a constant-density atmosphere for run D01 ( $M = 10$ ,  $\eta = 2 \times 10^{-4}$ ). The grid size is  $66 \text{ kpc} \times 79 \text{ kpc}$ .

The final stage of the simulation of run D01 is shown as a density contour map in Figure 19. After comparing this with runs D02 and D03, we concluded that no significant change is observed in the source physical properties, although their general appearance may look different. Therefore, in what follows, we show the results for run D01 only. In Figure 20a, we show the contours of the bow shock, cocoon, and jet. Figure 20 also shows the average pressure inside the cocoon (Fig. 20b), the lateral expansion speed of the cocoon (measured at the contact discontinuity; Fig. 20c), and the lateral expansion speed of the bow shock (measured at the outer shock front; Fig. 20d) along the source axis.

The average pressure was obtained in the following way. For each slice, with width equal to the grid cell and cylindrical symmetry, the total thermal energy was calculated by summing the product of the energy density per cell times the volume element of the cell and then dividing by the total volume of the slice to obtain the total internal energy density,  $0.5 \rho v_{\text{rms}}^2$  or  $3/2nkT$ . This was then multiplied by  $\Gamma - 1$  to obtain the average pressure in that cell. The simulations were carried out for an ideal monotonic, nonrelativistic fluid; thus, the ratio of specific heats is  $\Gamma = 5/3$ .

The shock structure seen in the numerical simulation is shown in Figure 20a. As usual, three shock regions can be identified: the outer shock front, the contact discontinuity, and the inner shock, which includes the entire bridge region.

In the simulation, the location of the jet can also be identified. The outer shock front is also called the bow shock and is indicated by the outermost line in Figure 20a. The contact discontinuity separates the shocked ambient gas from the shocked jet fluid and is indicated by the middle line in Figure 20a. The radio-emitting fluid that would produce the observed radio emission is expected to lie within the contact discontinuity. Thus, the

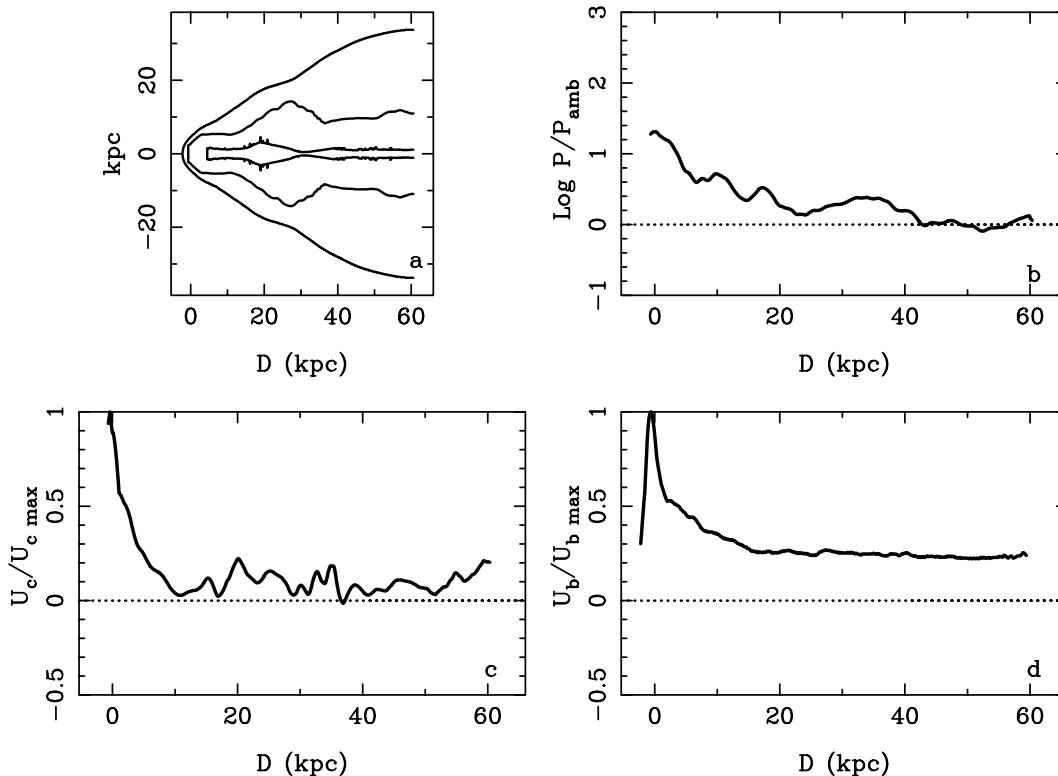


FIG. 20.—(a) Contour of the bow shock, cocoon, and jet for the simulation shown in Fig. 19 (run D01); (b) longitudinal profile of the average cocoon pressure; (c) cocoon lateral speed; (d) bow shock lateral speed.

region interior to the middle line in Figure 20a is referred to as the “cocoon” throughout this paper. The shocked ambient gas lies between the bow shock and the cocoon and is not discussed further in this paper. The jet is identified in the simulations by means of trace particles that are injected together with the jet gas.

Slices are taken across the cocoon, and the average pressure within the cocoon is computed for each slice as described above. This average pressure is plotted as a function of distance from the hot spot in Figure 20b and is normalized to unity at the location of the hot spot. This measure of the pressure includes only the thermal pressure of the “gas” within the cocoon of the numerical simulation and does not include kinetic pressure. In the numerical simulation, the average pressure in slices across the cocoon undergoes a series of oscillations as we move along the symmetry axis of the bridge.

The lateral expansion of the cocoon (i.e., as defined by the contact discontinuity) and that of the bow shock are shown in Figures 20a and 20c and are normalized to unity at the location of the hot spot. Like the bridge width and the average pressure in a slice across the bridge (i.e., the cocoon), the lateral expansion speed of the cocoon undergoes a series of oscillations rather than varying smoothly along the contact discontinuity. This variation in its lateral expansion speed is reflected in differences in the bridge width. For example, in the simulation, the bridge width has a bulge at distances from the hot spot of about 10–30 kpc, corresponding to a region with an increase in the lateral expansion speed of the cocoon relative to nearby points. The lateral expansion speed of the bow shock varies much more smoothly and monotonically with distance from the hot spot and generally appears to follow  $U_b \propto D^{1/2}$ , which is theoretically predicted for the regions where the expansion speed exceeds the ambient sound speed, after which the expansion speed is expected to level off (e.g., Begelman & Cioffi 1989; Daly 1990, 1994; Wellman et al. 1997a; Reynolds et al. 2002; Carvalho & O’Dea 2002a).

### 3.2. Dynamical and Synchrotron Age

The ratio between the source advance speed and the initial jet speed is shown in Figure 21 as a function of source size. For comparison, we also show the ambient sound speed (*dashed line*). We see how the source decelerates rapidly with its Mach number relative to the ambient sound speed, decreasing by a factor of  $\sim 22$  from  $\sim 70$  to  $\sim 3.2$ . This is because of the progressive increase of the jet head radius. The observed speed fluctuations are also due to oscillations of the head radius. These oscillations of the head radius are probably driven by vortex shedding (e.g., Lind et al. 1989; Norman et al. 1982). We note that changes in jet momentum flux may also drive changes in the advance speed. Near the end of the simulation, an increase is observed in the advance speed, which experience indicates is a transient phenomenon.

Two effects likely to occur in nature that are not included in the simulation may also come into play. In nature, the density of the ambient gas may slowly decrease with distance from the central engine rather than remain constant, and this would cause the decline in the head velocity to be less significant. On the other hand, in nature the outflow axis of the jet may “wobble” rather than point in a fixed direction (as in the simulation), which would have an effect in the opposite sense and at any given time would decrease the velocity of the head (e.g., Scheuer 1982; Cox et al. 1991). This second effect could also modify the bridge width as a function of distance from the hot spot.

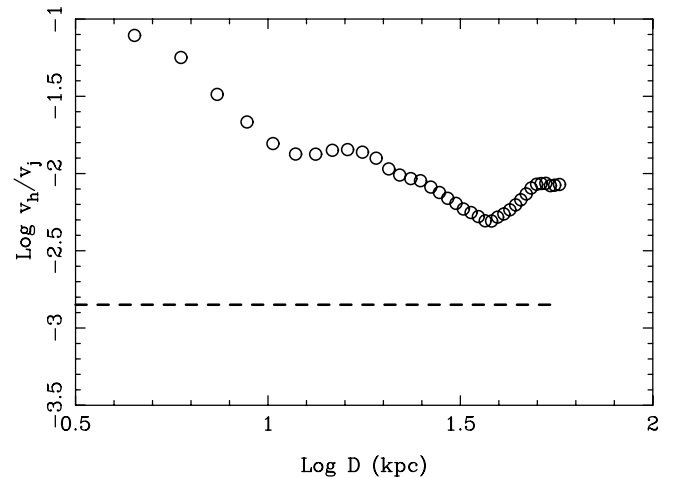


FIG. 21.—Advance speed of the head (*circles*) relative to the jet initial speed as a function of source size. The dashed line represents the ambient sound speed.

The dynamical age of Cyg A determined using the ram pressure of the hot spot is about an order of magnitude larger than the estimated synchrotron age (Carilli et al. 1991). It has been suggested by some authors that this discrepancy can be alleviated if one relaxes the equipartition hypothesis when estimating the magnetic field. According to Carilli et al., the magnetic field must be one-third of the equipartition value. Similar results have been found by Perley & Taylor (1991) for 3C 295 and by Wellman et al. (1997a, 1997b) for a large sample of sources. The deceleration of the source head observed in the simulations can, at least in part, be responsible for the discrepancy.

Thus, the age calculated using the speed at the source maximum length is larger than the real age of the source. In our simulation, the difference is not too large because at the end of the simulation the head speed momentarily increases. However, if we calculate the age by taking the head speed when the source, for instance, is  $\sim 51$  kpc in size, it would be larger than the real age by a factor  $\sim 2$ . Thus, this effect can account for only a part of the discrepancy between the ram pressure balance and synchrotron ages found by Carilli et al. (1991).

### 3.3. Surface Brightness and Radio Emissivity

We have calculated the volume emissivity of the source by assuming that the energy density of the relativistic electron component is proportional to the hydrodynamic (thermal) pressure of the gas inside the cocoon and an equipartitioned magnetic field. This is easy to do since the radio emissivity is proportional to  $P^{7/4}$ , as described at the end of § 2.4. We also consider separately the contributions proportional to the thermal pressure, the kinetic pressure, and the total pressure (see Fig. 25). We assume that the radio emission comes from the jet itself and the cocoon (Leahy 1991), where the pressure is higher than the ambient pressure. This region (corresponding to the region interior to the middle line in Fig. 20a) is filled with jet material that has been shocked in the head and expands laterally. Besides any non-relativistic gas that may be present in this region, it is assumed that the region also contains the basic ingredients necessary to generate synchrotron emission, that is, a mixture of magnetic field and relativistic electrons most probably accelerated by the Fermi process at the strong shock region in the jet head. We integrated the radio emissivity along the line of sight (assuming the source lies in the plane of the sky) to obtain the surface

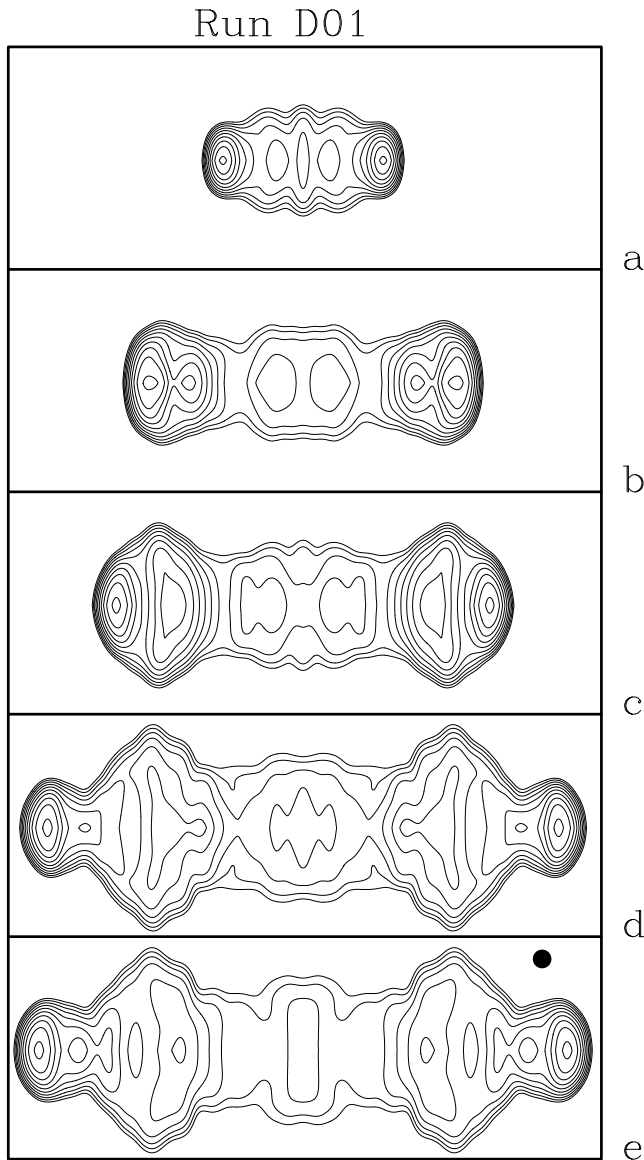


FIG. 22.—Synthetic radio image showing the time evolution of the numerical simulation of a jet ( $M = 10$ ,  $\eta = 2 \times 10^{-4}$ ) propagating in a constant-density atmosphere. Each panel measures  $144 \text{ kpc} \times 54 \text{ kpc}$ , and the synthetic data have been smoothed by a Gaussian with an FWHM of  $3''$  to match the 151 MHz data, as shown by the circle in (e). The age of the source corresponding to each stage is (a) 1.35, (b) 4.53, (c) 6.17, (d) 8.89, and (e) 9.15 Myr. One can clearly see the characteristic edge-brightened shape of powerful FR II sources and an aspect ratio resembling that of Cyg A.

brightness, which allows us to draw synthetic radio images of the source. We have also taken into account radiation loss of the relativistic electron population in a very simple way. We divided the cocoon into slices and assigned an age to each slice equal to the time that has passed since it was laid down by the advancing jet head. The modified spectrum is then calculated using the Kardashev-Pacholczyk model (Kardashev 1962; Pacholczyk 1970), supposing that the magnetic field is the equipartition field.

In this manner, we were able to predict the radio structure that would be observed from the source indicated by the numerical simulation. In Figure 22 we show the predicted 151 MHz radio image of the source at five evolutionary stages; the synthetic data have been smoothed by a Gaussian with an FWHM of  $3''$  to match the 151 MHz data, as shown by the circle in Figure 22e.

The age of the source corresponding to each evolutionary stage in Figure 22 is (a) 1.35, (b) 4.53, (c) 6.17, (d) 8.89, and (e) 9.15 Myr. One can clearly see the characteristic edge-brightened shape of powerful FR II sources and an aspect ratio resembling that of Cyg A. When the source is young, radiative energy losses are negligible, and we can see the radio bridge extending all the way from the head to the central galaxy (Figs. 22b and 22c). As the source ages, the central parts become less luminous, and it assumes the classical double-lobe shape (Fig. 22e). The hot spots are evident in all the simulated images.

Cross-sectional slices of the surface brightness distribution for the source as it appears in Figure 22e, when it is about 9 Myr old, are shown in Figure 23. The second panel in the first row corresponds to the position of the hot spot, while the bottom rows show the parts of the source near the central object. We have normalized the surface brightness to unity at the hot spot, and the scale in each row is the same as that in Figure 4 at 151 MHz. The simulated surface brightness is qualitatively similar to that observed in Cyg A (Figs. 2–5). Of course, the simulation is axisymmetric, and thus so are the cross-sectional surface brightness slices, whereas in nature this is not always the case.

The Gaussian fit is shown as dotted lines in Figure 23. The central spikes that appear in some of the panels are caused by the jet's contribution to the surface brightness. The spikes are more evident in those regions of the jet where it has been compressed (Fig. 19). The Gaussian fits provide a reasonable approximation of the actual surface brightness slices over most of the source except along the third row, where the wings of the Gaussian fit clearly extend well beyond the boundary of the source.

Figure 24 shows the predicted average surface brightness of a slice as a function of distance from the hot spot in the numerical simulation; the average surface brightness is obtained as described in § 2.3 but using the true width of the simulated source.

Here we investigate how the different forms of energy (thermal pressure, kinetic pressure, and total pressure) could contribute to the radio emission. Again, the pressure from relativistic electrons and magnetic fields is assumed to be proportional to the gas pressure, as determined by the local thermal pressure, kinetic pressure, or total pressure given by the numerical simulation. The thermal pressure is the thermodynamic pressure associated with the gas microscopic motion (discussed in § 3.1). The kinetic pressure is equal to  $\Gamma - 1$  times the kinetic energy density, where the kinetic energy density  $0.5\rho v^2$  depends on the large-scale, macroscopic, or bulk velocity  $v$  of the gas. The total pressure is the sum of the thermal and kinetic pressures. We also use the approximation that the emissivity is proportional to  $P^{7/4}$  (described in § 2.4). Considering the kinetic pressure allows for the fact that macroscopic kinetic energy in the form of turbulent motion could be transferred to the relativistic component through the Fermi process or through hydromagnetic instabilities (e.g., De Young 1980; Eilek & Henriksen 1984; Eilek & Shore 1989). For this figure, the radio emissivity is calculated by supposing that the local pressure of the relativistic fluid, including that from the relativistic electrons and magnetic fields, is equal to the total pressure (*solid line*), thermal pressure (*dash-dotted line*) and the kinetic pressure (*dotted line*).

We observe that in many places the contribution of the kinetic pressure can be very important. This feature is not considered by the majority of works in the literature. It is very interesting to note that the surface brightness profile indicated by the total pressure (kinetic plus thermal) is very similar to that of the 151 MHz data (see Fig. 11). The surface brightness profile

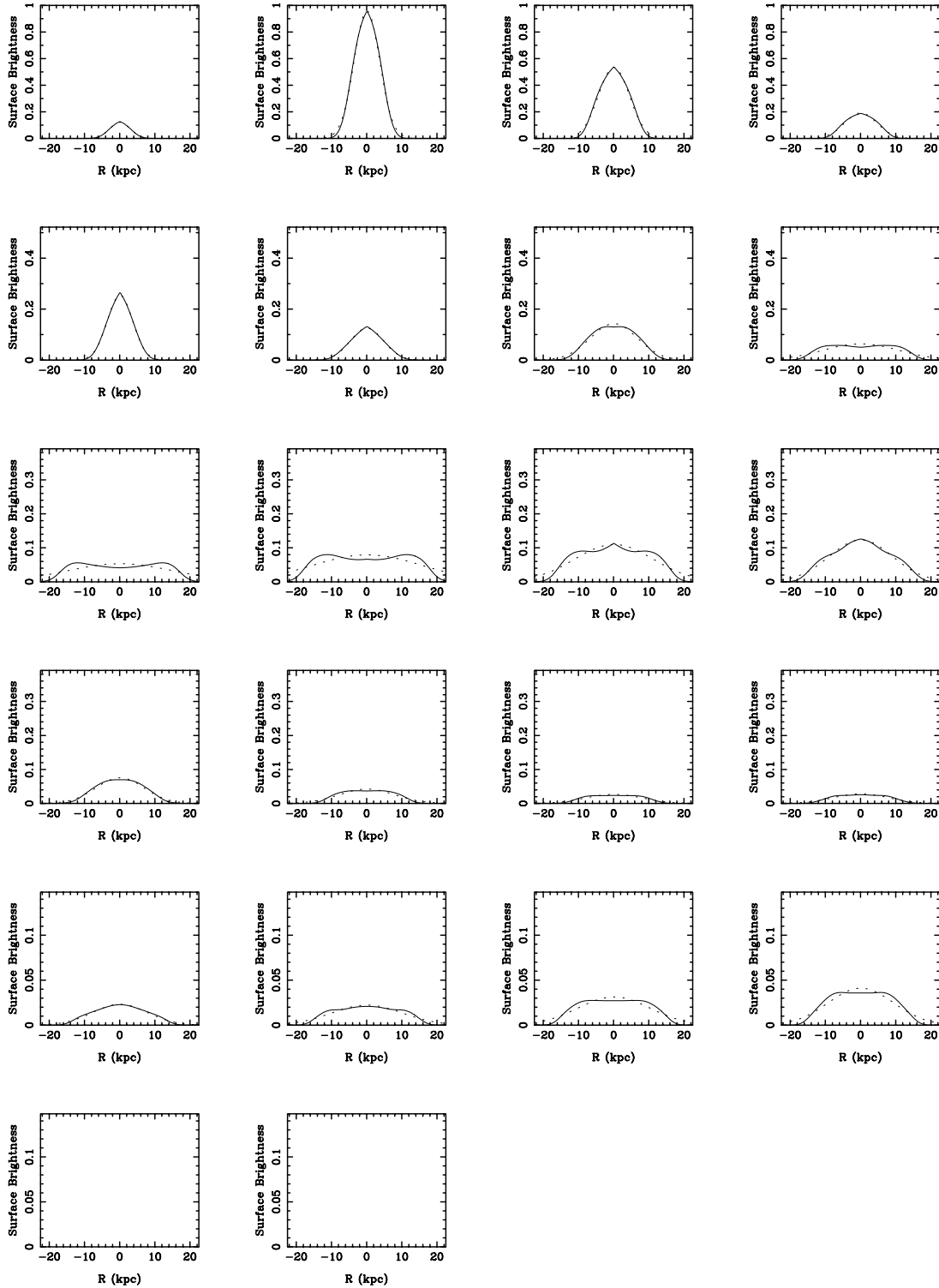


FIG. 23.—Cross-sectional surface brightness profiles (*solid lines*) and Gaussian fits (*dotted lines*) for the numerical simulation (run D01). The distance between panels is 3 kpc.

indicated by the thermal pressure alone is very similar to that of the 1345 MHz data (see Fig. 11). This suggests that different forms of energy within the bridge may enhance radio emission differently at different frequencies. It is easy to see how this could occur since the radio emission at different frequencies is produced by relativistic electrons with different Lorentz factors. Thus, it would require only that the thermal pressure produce an underlying relativistic electron population with a power-law

distribution at all Lorentz factors, while the kinetic pressure boosts additional relativistic electrons to Lorentz factors that produce the 151 MHz emission but not the 1345 MHz emission. For example, through hydromagnetic processes the kinetic pressure could boost relativistic electrons with lower Lorentz factors up to the Lorentz factors needed to produce 151 MHz emission. This could help explain some of the changes in the radio spectrum seen across the source.

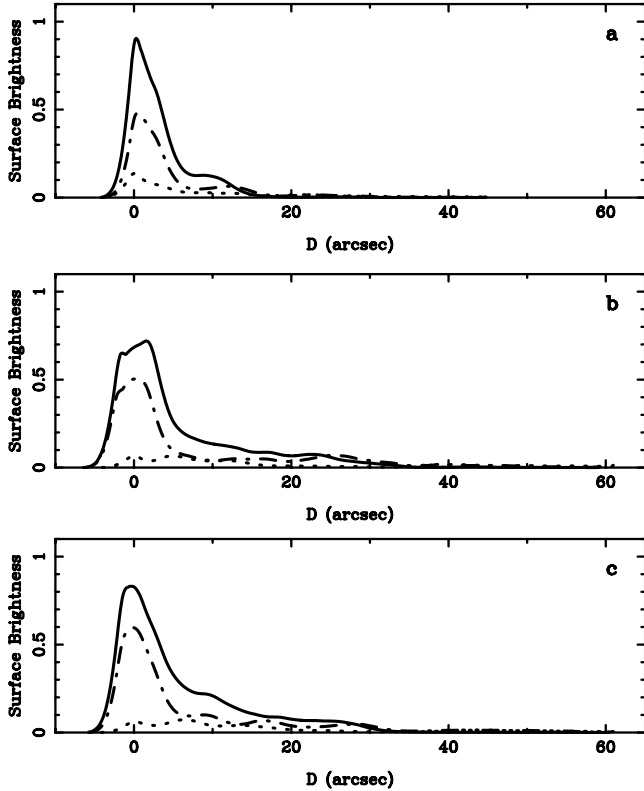


FIG. 24.—Average surface brightness at 151 MHz in a cross-sectional slice as a function of distance from the hot spot, taking into account radiative losses. The radio emissivity is calculated by supposing that the relativistic electron density is proportional to the total pressure (*solid line*), thermal pressure (*dash-dotted line*), and the kinetic pressure (*dotted line*). Panels *a*, *b*, and *c* correspond to panels *c*, *d*, and *e* of Fig. 22, respectively.

To investigate this further, we compare the average thermal pressure and the total average pressure (thermal plus kinetic pressures) obtained from the numerical simulation with the average pressure obtained from the 151 and 1345 MHz data (Fig. 25). To do this, the physical value of the units of the pressure obtained from the simulation were investigated and were determined to be  $1.596 \times 10^{-8} n_a \text{ dyn cm}^{-2}$ , where  $n_a$  is the ambient gas density. A value of  $n_a = 10^{-2} \text{ cm}^{-3}$  was adopted since this is consistent with X-ray measurements of the gas in the vicinity of the radio source (e.g., Smith et al. 2002). The behavior of the pressures in the simulations roughly tracks that seen in the data. Of course, it is possible that the value of  $b$  in the hot spot region is closer to unity (e.g., Hardcastle et al. 2002, 2004; Donahue et al. 2003; Wilson et al. 2000), while that in the bridge is  $\sim 0.25$ . (e.g., Carilli et al. 1991; Perley & Taylor 1991; Wellman et al. 1997b). The value of  $b$  does not affect the pressures determined using the numerical code (which depend only on the scaling factor  $n_a$ ), but it does affect the pressure determined from the data. If  $b$  in the hot spot is closer to unity, then the pressure determined using the data is lower in this region than the values shown. This would improve the fit to the 1345 MHz data and worsen the match with the 151 MHz data. Another effect to consider is the efficiency factor (converting gas kinetic energy into relativistic energy) used to convert surface brightness to pressure, which could vary with location within the source or could depend on energy, resulting in a dependence on frequency. In addition, consider that particle reacceleration within the bridge region or a backflow could be important in the source. In view of these factors, the rough overall agreement between the data and the simulation is encouraging.

Finally, in Figure 26 we compare the thermal pressure determined from the simulation at several different times with that estimated from the 151 MHz empirical data for the two sides of

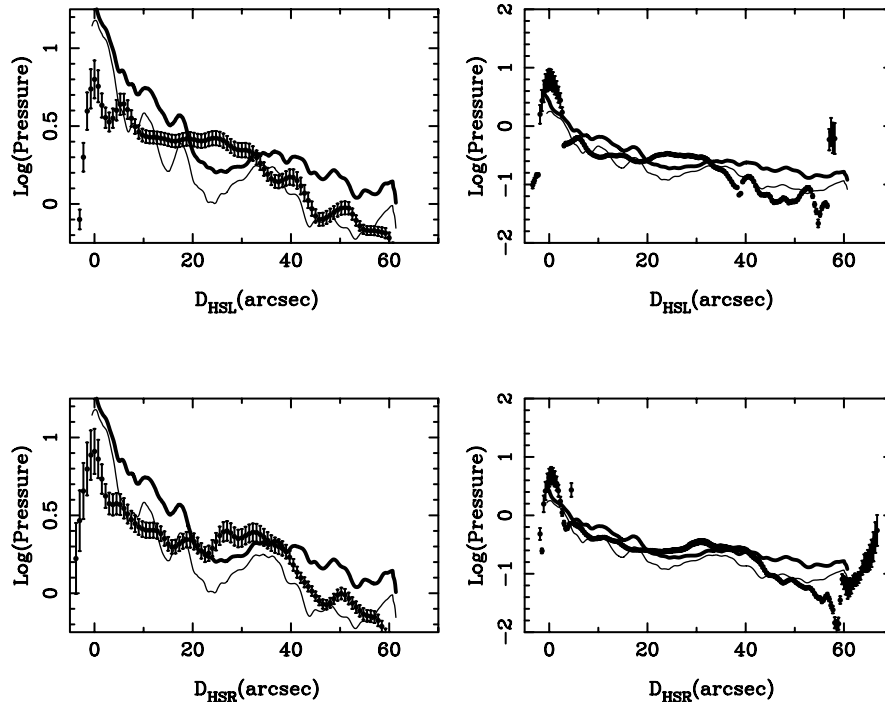


FIG. 25.—Comparison between the logarithm of the observed and calculated average total pressure (thermal plus kinetic; *thick line*) and thermal (*thin line*) pressure as a function of distance from the hot spot for 151 (*left*) and 1345 MHz (*right*). *Top*, Left side of the source; *bottom*, right side of the source. The calculated pressure is that for an ambient density of  $n_a = 0.01 \text{ cm}^{-3}$ , and the units of pressure are the same as in Fig. 12 for the value of the parameter  $b$ , which defines the offset from minimum-energy conditions, equal to 0.25. Thus, the units of the 151 MHz pressure are  $1.3 \times 10^{-10} \text{ ergs cm}^{-3}$ , while those of the 1345 MHz pressure are  $1.1 \times 10^{-9} \text{ ergs cm}^{-3}$ .

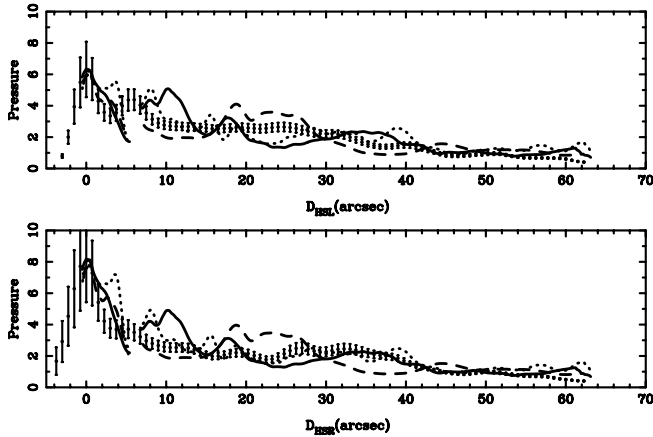


FIG. 26.—Comparison between observed and calculated average thermal pressure as a function of distance from the hot spot, with the numerical result scaled to match the empirical result at the hot spot peak. *Top*, Left side of the source; *bottom*, right side of the source. The dashed, dotted, and solid lines correspond to panels *c*, *d*, and *e* of Fig. 22, respectively.

Cyg A, each normalized to match at the peak of the hot spot. Sources are dynamic, constantly changing with time, so we consider snapshots corresponding to Figures 22*c*, 22*d*, and 22*e*, rescaled to a length of 60 kpc. The dynamic nature of the source is obvious from these snapshots. The agreement is better than for the surface brightness distribution, because the simulated pressure profile does not depend on the bridge width. As we see below, the simulated and observed width do not agree equally well over the entire extent of the bridge. We see that the pressure profile varies considerably with time over the course of the simulation. This implies that there is no “steady state” pressure distribution in the lobes.

#### 3.4. Bridge Width

We compare the “true” width of the bridge in the simulation (Fig. 20*a*) with the FWHM and second moment of the synthetic surface brightness distribution (Fig. 27), where only the thermal component of the surface brightness was considered. We find that, while the second moment gives a good fit to the true cocoon width, the Gaussian FWHM deviates significantly. (Note that this is not seen in the data, in which the second moment and FWHM of the Gaussian fits track each other quite well; Fig. 10.) The main departure in the simulation occurs between 20 and 30 kpc from the hot spot. This can be attributed to the fact that the cross-sectional slices of the surface brightness distribution in this region exhibit a double peak, as can be seen in Figure 23. This double peak implies that the gas pressure distribution inside the simulated cocoon is higher near its edges, at least in the region in question (20–30 kpc).

The ratio  $\zeta = W_G/W_2$  between the two quantities is in the range  $\sim 1.2$ – $1.8$ , with an average value of  $1.39 \pm 0.07$ . For a perfect Gaussian distribution, the ratio  $\zeta = (2 \ln 2)^{1/2} \simeq 1.177$ . To compare this with the empirical data shown in Figure 10, we note that in this figure we plotted  $2\zeta = W_G/(\text{second moment})$ ; recall that  $W_2 = 2 \times (\text{second moment})$ . Since the value of the empirical data is in the range 2–3, we conclude that the results of the simulations,  $2\zeta \sim 2.4$ – $3.6$ , are in fair agreement with the data.

Figure 28 shows a comparison between the observed FWHM of the radio source and the “true” width of the simulated source. We see that the simulation shows the same general behavior as the radio source.

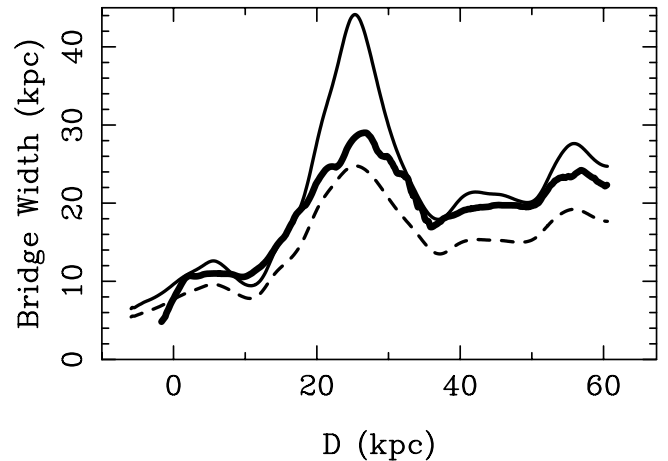


FIG. 27.—Bridge width calculated from the Gaussian fit (FWHM) and the second moment, compared with the full width of the cocoon measured from the simulations, as a function of distance from the hot spot and showing the cocoon ( $W$ ; thick line), the Gaussian fit ( $W_G$ ; thin line), and the second moment ( $W_2$ ; dashed line).

#### 3.4.1. Emissivity Distribution

As mentioned above, the value of the ratio  $\zeta = W_G/W_2$  depends on the emissivity distribution across the cocoon. In this sense, the ratio may be used as a diagnostic of the distribution of emissivity.

We have thus investigated this by calculating the ratio  $\zeta$  for a simple model cocoon whose radius varies smoothly, according to

$$R_c = 0.5 + 9.5 \left( \frac{D}{60 \text{ kpc}} \right)^{1/2},$$

where  $D$  is the distance from the hot spot and  $R_c$  is in kiloparsecs. We studied five cases with different pressure profiles  $P(r)$ . The radial dependence of  $P$  is shown in Table 1. In all cases  $P = 0$  for  $r > R_c$ ;  $r$  is measured from the symmetry axis of the source.

We calculated the surface brightness using the same beam size as for the empirical data, calculated the second moment, and fitted a Gaussian to the surface brightness profile perpendicular to the cylinder axis to determine the ratio  $\zeta$ . The values of  $W$ ,  $W_G$ , and  $W_2$  for four of the model bridges in Table 1 are shown in Figure 29. We can clearly see how the relation between the true width  $W$  and the calculated ones  $W_G$  and  $W_2$  depends strongly on the pressure distribution across the cocoon.

In Table 1 we show the average values of the Gaussian width, the second moment, and  $\zeta$  for the five distributions. We see that for model A both the Gaussian fit and the second moment are about 55%–70% of the true width and thus need to be normalized to be used as a direct measure of the bridge width. For the other models, the Gaussian width increasingly departs from the true width as the peak of pressure distribution moves away from the source axis. On the other hand, the second moment gives a better estimate when the pressure distribution concentrates near the border of the cocoon.

We note that the range of values of the ratio  $\zeta$  of the Gaussian FWHM and that of the second-moment width  $W_2$  for the five distributions are in agreement with the value from the numerical simulations (1.2–1.8). The average value observed in Cyg A ( $\sim 2.5 = 2 \times 1.25$ ) is compatible with an emissivity distribution concentrated near the source axis (model A). In a few cases when it reaches higher values ( $\sim 3 = 2 \times 1.5$ ), the

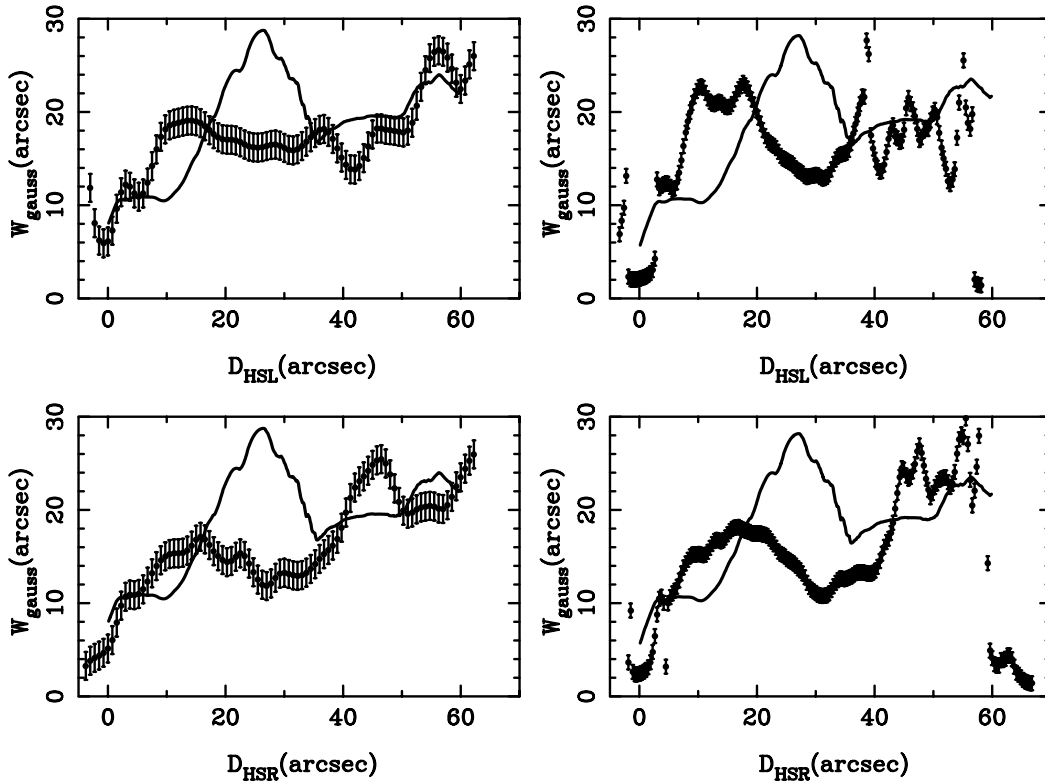


FIG. 28.—Comparison between the FWHM fit to the radio data with the “true” width of the simulated source as a function of distance from the hot spot for 151 (left) and 1345 MHz (right). Top, Left side of the source; bottom, right side of the source.

pressure distribution in these regions must have two separate peaks, as in model E. In fact, if we look at the deconvolved emissivity distribution of Cyg A at 151 MHz (Figs. 15–18), we see that this seems indeed to be the case in several sections of the bridge. Thus, the ratio between the Gaussian width and the second moment can provide a diagnostic of the emissivity profile in the lobe. It may be necessary to run three-dimensional numerical simulations to properly “calibrate” this diagnostic ratio.

We have seen that for the numerical simulation the second moment of the surface brightness distribution gives a more stable estimate of the bridge width in our model cocoon than that of the Gaussian fit (e.g., Fig. 27). If this applies to real sources, it can be used as a measure of its real width, provided we have a proper normalization factor. Our simulation gives an average value for the ratio between the cocoon and Gaussian width  $\beta_G = W/W_G$  of  $\beta_G = 0.91 \pm 0.12$ , while the average ratio of the true width to the second moment,  $\beta_2 = W/W_2$ , is  $\beta_2 = 1.26 \pm 0.04$ , where  $W_2 = 2 \times (\text{second moment})$ .

We note that (using  $\zeta = W_G/W_2$  as a diagnostic; Table 1) the range of values of  $\zeta$  found in Cyg A indicates that at least in some regions the bridge has high-pressure edges. Carilli et al.

(1991) suggest that an edge brightening of the lobes could account for the increase in the magnetic field from the center to the edge of the lobes needed to explain the estimated age gradient. If this is the case, the Gaussian fit overestimates the bridge width in models D and E (Table 1), and, again, the second moment should be used to calculate the bridge width.

4. SUMMARY

We present a comparison of radio observations of the powerful archetypal radio galaxy Cyg A and two-dimensional numerical hydrodynamic simulations. We characterize some global trends in the observed radio properties and compare them with the properties of a simulated radio source. We have analyzed detailed radio images at 151 MHz (Leahy et al. 1989) and 1345 MHz (Carilli et al. 1991). We have determined the surface brightness, emissivity, Gaussian FWHM, and the first and second moment of cross-sectional slices of the source as a function of distance along the bridges. We have also estimated the average pressure and minimum-energy magnetic field in the radio plasma as a function of distance along the bridges. We find the following trends in global properties:

TABLE 1  
COMPARISON BETWEEN CALCULATED AND TRUE WIDTH FOR A MODEL BRIDGE

Model	Pressure Distribution $P(r)$	Gaussian Fit $\langle W_G/2R_c \rangle$	Second Moment $\langle W_2/2R_c \rangle$	$\langle \zeta = W_G/W_2 \rangle$
A.....	$1 - (r/R_c)$	0.673	0.550	1.223
B.....	1	1.075	0.786	1.367
C.....	$(r/R_c)^{1/2}$	1.211	0.848	1.428
D.....	$(r/R_c)^1$	1.301	0.889	1.463
E.....	$(r/R_c)^2$	1.416	0.939	1.507

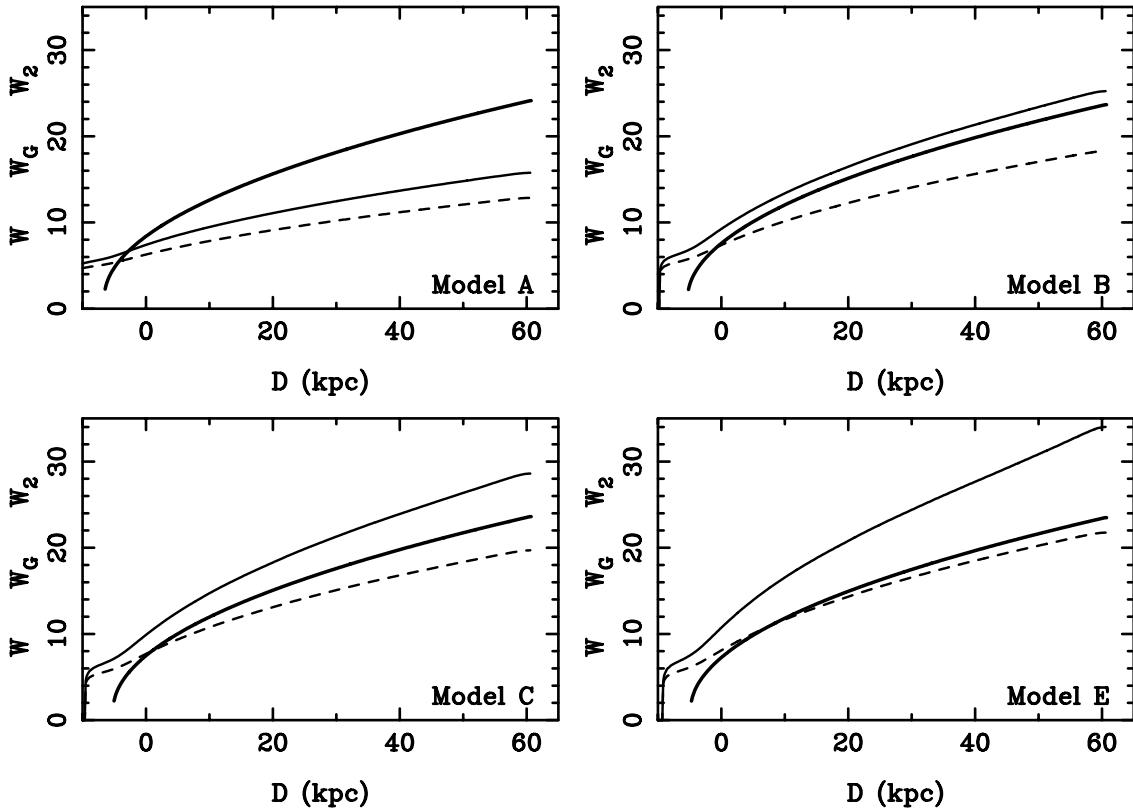


FIG. 29.—Bridge width calculated from the Gaussian fit (FWHM) and the second moment, compared with the full width of the model cocoon, as a function of distance from the hot spot and showing the cocoon ( $W$ ; thick line), the Gaussian fit ( $W_G$ ; thin line), and the second moment ( $W_2$ ; dashed line). The four panels represent models in Table 1.

1. The first moment of the brightness distribution perpendicular to the source axis is a measure of the surface brightness-weighted center of the source. We find that the first moment wanders, with a peak-to-peak amplitude of  $\sim 10''$ . The sense of the wandering has opposite signs on each side of the source, but there is not an exact correspondence.

2. The width of the surface brightness distribution perpendicular to the source axis can be well characterized by a Gaussian over most of the length of the source. The ratio of the Gaussian FWHM to the second moment is fairly constant along the source, with an average value of about 2.5, indicating that they give roughly consistent measurements of the source width. The radio lobe increases in width with distance from the hot spot. Superposed on this general expansion are several wiggles.

3. The average surface brightness, estimated pressure, and estimated minimum-energy  $B$ -field decrease with distance from the hot spots.

4. We find evidence for significant structure in the estimated cross-sectional slices of emissivity.

Following the methods of Carvalho & O’Dea (2002a, 2002b), we present the results of two-dimensional numerical hydrodynamic simulations of light (density contrast  $\zeta = 10^{-4}$ ), supersonic (jet Mach number  $M = 10$ ) jets propagating in a constant-density environment. The results from the simulations are the following:

1. Jets propagating in a constant-density atmosphere decelerate with time (see also Carvalho & O’Dea 2002a). Thus, the estimated dynamical age of the source is greater than the actual age of the source. For a source similar to Cyg A, the difference is about a factor of 2.

2. We ran the simulations with several different grid widths. In the largest grid, the entire source was contained in the grid, while in the smaller grids, the bow shock eventually moved laterally off the grid. We find that the details of the cocoon properties differ in these simulations, although the overall properties of the cocoons are similar.

3. The pressure profile varies considerably with time over the course of the simulation. This implies that there is no steady state pressure distribution in the lobes. There is considerable time dependence in the variation of the average surface brightness in the lobe near the hot spots, possibly due to vortex shedding.

4. The kinetic pressure in the cocoon (due to large-scale turbulence) can make a significant contribution to the total pressure of the cocoon. We speculate that the thermal pressure produces an underlying relativistic electron population with a power-law distribution at all Lorentz factors, while the kinetic pressure adds “extra” relativistic electrons with the Lorentz factors that produce the 151 MHz emission and not the 1345 MHz emission. For example, through hydromagnetic processes, the kinetic pressure could boost relativistic electrons with lower Lorentz factors up to the value of the Lorentz factor needed to produce the 151 MHz emission. This could help explain some of the changes in the radio spectrum seen across the source.

5. The second moment gives an accurate representation of the “true” width of the simulated source. The Gaussian FWHM tends to be about 40% larger than the true width and can be systematically in error if the surface brightness exhibits multiple peaks. We suggest that the ratio of the Gaussian FWHM to the second moment may be a diagnostic of the emissivity profile in the lobes. However, “calibration” of this diagnostic probably requires three-dimensional simulations. Applying this diagnostic

reveals that the bridge has high-pressure edges. This is consistent with the suggestion of Carilli et al. (1991) that an edge brightening of the lobes could account for the increase in the magnetic field from the center to the edge of the lobes, which is needed to explain the estimated age gradient.

We compare our simulations with the properties of the observed radio sources in two complementary ways. We note that the pressure is directly determined in the simulation but is estimated from the radio data, while the surface brightness is directly determined from the radio data but is estimated from the simulations.

The simulations can qualitatively reproduce the overall observed morphology and the behavior of the cross sections in surface brightness, the decline in surface brightness with distance from the hot spots, and the width of the lobes. This suggests that the two-dimensional simulations give a reasonable representation of the properties of Cyg A.

This is especially encouraging, given that the outflow axis of the jets in Cyg A may wobble, while those in the numerical simulation were held steady, and that the ambient gas density in the simulation is assumed to be constant. The good agreement between the simulation and the data suggests that these effects are relatively small for a source such as Cyg A.

We are grateful to Paddy Leahy and Chris Carilli for sending us their radio data and to the referee for a thoughtful review of the manuscript. J. C. C. acknowledges the financial support of PRONEX/Finep and CNPq and the hospitality of the Space Telescope Science Institute (STScI), where this work was carried out. This work was supported in part by a grant to C. P. O. from the STScI Collaborative Visitor Program, which funded visits by J. C. C. to STScI, and by grant AST 02-06002 to R. D. from the National Science Foundation.

#### REFERENCES

- Alexander, P., & Leahy, P. 1987, *MNRAS*, 225, 1  
 Alexander, P., & Pooley, G. G. 1996, in *Cygnus A: Study of a Radio Galaxy*, ed. C. L. Carilli & D. E. Harris (Cambridge: Cambridge Univ. Press), 149  
 Begelman, M. C., & Cioffi, D. F. 1989, *ApJ*, 345, L21  
 Blandford, R. D., & Rees, M. J. 1974, *MNRAS*, 169, 395  
 Burbidge, G. R. 1956, *ApJ*, 124, 416  
 Carilli, C. L., Perley, R. A., Dreher, J. W., & Leahy, J. P. 1991, *ApJ*, 383, 554  
 Carvalho, J. C., & O'Dea, C. P. 2002a, *ApJS*, 141, 337  
 ———. 2002b, *ApJS*, 141, 371  
 Cioffi, D. F., & Blondin, J. M. 1992, *ApJ*, 392, 458  
 Clarke, D. A., & Burns, J. O. 1991, *ApJ*, 369, 308  
 Clarke, D. A., Norman, M. L., & Burns, J. O. 1986, *ApJ*, 311, L63  
 ———. 1989, *ApJ*, 342, 700  
 Cox, C. I., Gull, S. F., & Scheuer, P. A. G. 1991, *MNRAS*, 252, 558  
 Daly, R. A. 1990, *ApJ*, 355, 416  
 ———. 1994, *ApJ*, 426, 38  
 De Young, D. S. 1980, *ApJ*, 241, 81  
 Donahue, M., Daly, R. A., & Horner, D. J. 2003, *ApJ*, 584, 643  
 Eilek, J. A., & Henriksen, R. N. 1984, *ApJ*, 277, 820  
 Eilek, J. A., & Shore, S. N. 1989, *ApJ*, 342, 187  
 Falle, S. A. E. G. 1991, *MNRAS*, 250, 581  
 Hardcastle, M. J., Birkinshaw, M., Cameron, R. A., Harris, D. E., Looney, L. W., & Worrall, D. M. 2002, *ApJ*, 581, 948  
 Hardcastle, M. J., Harris, D. E., Worrall, D. M., & Birkinshaw, M. 2004, *ApJ*, 612, 729  
 Hardee, P. E., & Norman, M. L. 1990, *ApJ*, 365, 134  
 Kardashev, N. S. 1962, *Soviet Astron.—AJ*, 6, 317  
 Komissarov, S. S. 1989, *ApJ*, 29, 619  
 Komissarov, S. S., & Falle, S. A. E. G. 1997, *MNRAS*, 288, 833  
 ———. 1998, *MNRAS*, 297, 1087  
 Krause, M. 2003, *A&A*, 398, 113  
 Leahy, J. P. 1991, in *Beams and Jets in Astrophysics*, ed. P. A. Hughes (Cambridge: Cambridge Univ. Press), 100  
 Leahy, J. P., Muxlow, T. W. B., & Stephens, P. W. 1989, *MNRAS*, 239, 401  
 Lind, K. R., Payne, D. G., Meier, D. L., & Blandford, R. D. 1989, *ApJ*, 344, 89  
 Loken, C., Burns, J. O., Clarke, D. A., & Norman, M. L. 1992, *ApJ*, 392, 54  
 Marti, J. M., Müller, E., Font, J. A., Ibanez, J. M., & Marquina, A. 1997, *ApJ*, 479, 151  
 Mioduszewski, A. J., Hughes, P. A., & Duncan, G. C. 1997, *ApJ*, 476, 649  
 Norman, M. L., Smarr, L., Winkler, K.-H. A., & Smith, M. D. 1982, *A&A*, 113, 285  
 Pacholczyk, A. G. 1970, *Radio Astrophysics: Nonthermal Processes in Galactic and Extragalactic Sources* (San Francisco: Freeman)  
 Perley, R. A., & Taylor, G. B. 1991, *AJ*, 101, 1623  
 Reynolds, C. S., Heinz, S., & Begelman, M. C. 2002, *MNRAS*, 332, 271  
 Rosen, A., Hughes, P. A., Duncan, G. C., & Hardee, P. E. 1999, *ApJ*, 516, 729  
 Scheuer, P. A. G. 1974, *MNRAS*, 166, 513  
 ———. 1982, in *IAU Symp. 97, Extragalactic Radio Sources*, ed. D. S. Heeschen & C. M. Wade (Dordrecht: Reidel), 163  
 Smith, D. A., Wilson, A. S., Arnaud, K. A., Terashima, Y., & Young, A. J. 2002, *ApJ*, 565, 195  
 Wan, L., Daly, R. A., & Guerra, E. J. 2000, *ApJ*, 544, 671  
 Wellman, G. F., Daly, R. A., & Wan, L. 1997a, *ApJ*, 480, 79  
 ———. 1997b, *ApJ*, 480, 96  
 Wilson, A. S., Young, A. J., & Shopbell, P. L. 2000, *ApJ*, 544, L27